School of Chemistry

Diamond Deposition using Pulsed DC Plasma CVD

Sarah Palmer

This thesis is submitted in partial fulfilment of the requirements for the Honours Degree of BSc at the University of Bristol

Supervisor: Professor Neil Fox

Second Assessor: Professor Paul May

Section: Physical and Theoretical Chemistry

Acknowledgements

Firstly, thank you to Professor Neil Fox for the creation of this project and his constant guidance and direction throughout. I would also like to thank Dr Liam Cullingford and Dr James Smith for their technical knowledge as well as unwavering kindness and support. Further thanks must be extended to Professor Paul May, who provided invaluable guidance throughout the project. Finally, thank you to Bristol Diamond Group in its entirety along with my fellow project students, for making my time spent in the group so enjoyable.

Abstract

Pulsed direct current chemical vapour deposition (pulsed DC CVD) is a technique whereby an applied voltage generates radicals from a CH_4/H_2 gas mixture. This facilitates large-area, heteroepitaxial, diamond thin-film deposition. Previous studies on the pulsed-DC CVD reactor in Bristol Diamond Laboratories were limited by plasma instability; subsequent modifications to the electrode cooling system necessitated a new operating power and pressure.

In this study, iterative optimisation found that conditions of 3.8 % CH_4, 170 Torr and 1800 W and 15 % area reduction by a thermal break were optimal for diamond deposition on Mo. This resulted in a high uniformity, (111) diamond film with a peak in the Raman spectrum at 1332 cm^{-1} (FWHM 9 cm^{-1}). Growth rate was 12.4 $\mu m\ h^{-1}$ on a 490 mm^2 circular deposition area.

An investigation into pulse ‘rest time’ was carried out between 15 % and 44 % of duty cycle. A decrease in ‘rest time’ increased the cathode temperature, increasing plasma stability up to the upper limit of cathode temperature, above which the film was amorphous carbon. A new methodology of variable rest time to control substrate and cathode temperatures independently was adopted. This methodology facilitated a four-hour growth on Mo, the longest growth run on this reactor to date. Closed chamber growth resulted in a low growth rate of 4.44 $\mu m\ h^{-1}$. A three-hour growth on Si was achieved, exhibiting a small 1332 cm^{-1} diamond peak and a significant graphitic signal in Raman spectroscopy. The film exhibited low uniformity due to the low thermal conductivity of Si. At the reactor’s inception, deposition on Si was deemed impossible. This study was able to achieve some growth on Si and observed no damage to the substrate.

Contents

1.Introduction 1
Significance of Diamond 1
Diamond Properties 1
Diamond Synthesis 2
CVD Growth Mechanism 3
Gas ratio for growth 5
Methods of radical activation 6
Direct Current (DC) CVD 7
Qualitative characteristics of a DC glow discharge 8
Pulsed DC CVD 9
Considering Substrates for Pulsed DC CVD 10
Literature Results from Pulsed DC CVD 11
Isotopically pure diamond 12
Beta Voltaic Diamond 'Batteries' 12
2. Project Aims 13
3. Experimental Methods 14
Theory of Spectroscopic and Characterisation Techniques 14
The Pulsed DC CVD Reactor 18
Growth Procedure 19
Reactor Operating Procedure 20
Summary of Growth Conditions 22
4. Results and Discussion 23
Optimisation for Plasma Stability 23
A Stabilised Plasma (Run 6) 24
Optimisation for Film Quality 26
Substrate Temperature 26
Optimised conditions (Run 17) 31
Closed Chamber Deposition (Run 18) 33
Silicon as a Substrate (Run 19) 36
Morphological Comparisons 38
5. Conclusions 39
Future work 40
References 42
Appendix 44

Table of Figures

Figure 1 - The crystal structure of diamond by unit cell and lattice structure, bond length 3.57 Å, compared to graphite lattice structure, intralayer and interlayer bond lengths 1.42 Å and 3.35 Å respectively. Figure from Reference 1. [1] 1

Figure 2 - The phase diagram of carbon stability showing pressure (GPa) against Temperature (K) where natural synthesis is shown at intermediate pressures and high temperatures whereas CVD diamond growth is low pressure low temperature. Figure from Reference 11. [11] 2

Figure 3 - The stepwise radical growth mechanism of CVD diamond. Figure from Reference 22. [22] 3

Table 1 – Adapted from Angus et al, the key enthalpy (kcal mol^{-1}) and free energy (kcal mol^{-1}) of key gas-diamond and gas-substrate reactions during CVD diamond growth. Reactions 1 – 6 occur in the gas phase and 7 – 9 occur with the substrate (S). (1 kcal = 4.184 kJ) [17] 4

Figure 4 - The Bachmann triangle of diamond growth. Most CVD occurs with only CH_4 and H_2 at 1 - 3 % methane.[4] 5

Figure 5 - Adapted from Reference 5, categorisation of radical activation techniques used for CVD diamond growth, with those performed in Bristol Diamond Laboratory highlighted in blue.[5] 6

Figure 6 - An exemplar hot filament CVD reactor from Reference 4.[4] 6

Figure 7 – A diagram of a Microwave CVD reactor from Reference 4.[4] 7

Figure 8 - Figure of simplified DC CVD reactor taken from reference 5. [5] 7

Figure 9 - Characteristics of a glow DC discharge from cathode to anode. From reference 30 (chapter 14) [30] 8

Figure 10 - A diagram of the pulsed-DC reactor present in the Bristol Diamond Laboratory built by Palubiski from Reference 22 [22] 10

Figure 11 - A schematic of a beta voltaic diamond ‘battery’, demonstrating the emission of beta electrons by ^{14}C diamond creating the current. Figure from reference 3. [3] 12

Table 2 – The electronic transitions of species in a H_2/ CH_4 plasma and their characteristic fluorescence wavelengths from reference 43 .[45] 14

Figure 12 - Confocal laser spectroscopy technique, using a scanning mirror and dichromatic mirror to focus laser onto a single plane of the sample. Figure from Reference 46.[48] 15

Figure 13 - Diagram of an SEM demonstrating acceleration of electron beam by anode, focusing by electromagnetic coils and detection of backscattered and secondary electrons. Figure adapted from reference 47.[49] 16

Figure 14 - The interaction between vibrational energy levels of a material and monochromatic incident photons either through Raman or Rayleigh scattering. Figure from reference 48 .[50] 16

Figure 15 – An Exemplar Raman Spectrometer where a Charge-Coupled Device (CCD) captures digital spectra. Figure adapted from Reference 49. [51] 17

Figure 16 - On the left, inside the chamber of the pulsed DC CVD reactor present in Bristol Diamond Laboratory showing the copper cooling jacket surrounding the anode along with the gas ring and cathode. On the right a diagram of the same reactor adapted from Reference 22 .[22] 18

Figure 17 - The pulsed DC CVD reactor in the Bristol Diamond Laboratory, nicknamed 'The Minion'. The dome shaped growth chamber and computer used to run LabView and visible. 18

Figure 18 - Image of Oxford Lasers, laser cutter system present in the Bristol Diamond Laboratory.. 19

Table 3 – A summary of the growth conditions (power, rest time, pressure, duration, thermal break and electrode gap) used in each run. 22

Figure 19 – On the left a plasma arc resulting from a 2° misalignment between electrodes Power: 1810 W Pressure: 180 Torr and resulting deposition on a 25 mm Mo substrate on the right.. 23

Figure 20 - A Raman of the deposition under the focus plasma arc in Run 3, demonstrating sharp D and G bands at 1350 cm^{-1} and 1580 cm^{-1} respectively. [53] ... 23

Figure 21 – The stable plasma from Run 6 (175 Torr, 1790 W). Photograph taken by Prof. Neil Fox. 24

Figure 22 - An Optical emissions spectrum showing H Balmer series, CH species and C_2 Swan bands of the plasma from Run 6, Figure 21. 25

Figure 23 - On the left a highly graphitic film deposited on a 25 mm Mo disk, significant delamination shown. On the right a Raman spectrum with no 1332 cm^{-1} diamond peak present.. 25

Figure 24 - 0.5 mm thick, 25 mm diameter Mo thermal breaks A to D with 0.16, 4, 15 and 40 % areas missing, respectively. 26

Figure 25 - On the left the uneven deposition on a Mo substrate after 75-minute growth (Run 8) and a diagram of uneven substrate placement due to rough edges on the right. 27

Figure 26 - Raman from centre of the deposition with a diamond peak at 1332 cm^{-1} baseline subtracted and FWHM 5 cm^{-1} 27

Figure 27 - Images of the plasma from thermal breaks A – D (shown in Figure 22), grown on 25 mm Mo substrates, 15.5 mm electrode gap, 2000 W, 170 Torr. 28

Figure 28 - Progression of an unstable plasma taken at 20, 50 and 70 minutes from left to right. Conditions: 1800 W, 180 Torr, ... 29

Figure 29 - Raman of Run 14 (blue) compared to Run 4 (red) relative intensity of 1332 cm^{-1} diamond peak higher in Run 14. 29

Figure 30 - Effect of cathode temperature on plasma stability Rest time 2.5 μs on left and 1.5 μs on right, exhibiting a hotter cathode and more even substrate at lower rest time, images taken at 90 and 95 minutes. Conditions: 170 Torr 1750 W. 31

Figure 31 - SEM of areas differing most in morphology, centre (left) vs edge (right) from Run 17 31

Figure 32 - Raman of resulting optimised film from Run 17, with 1332 cm^{-1} diamond peak (FWHM 9 cm^{-1}). 32

Figure 33 - Plasma photograph of closed chamber run, debris on the cathode and orange halo visible. Image taken at time 160 minutes. 33

Figure 34 - Intensity of the C_2 peak relative to H_β emission over time from the average of Run 16 and 17 in blue and the closed chamber (run 18) in red. 33

Figure 35 - SEM images of closed chamber growth on Mo substrate showing (100) facets growth of high uniformity from centre (left) to 2 mm from edge (right). Average facet width 3.5 μm 35

Figure 36 - Raman of deposition from closed chamber run, exhibiting a small 1332 cm^{-1} diamond peak and a large graphitic signal 35

Figure 37 - Plasma images of silicon substrate with T = 2.5 μs left and T = 3.0 μs right, showing localised heating on centre of substrate and disappearance of ‘orange halo’ with increased cathode cooling through rest time. 36

Figure 38 - SEM images of deposition on silicon substrate from centre (left) to edge (right) showing transition from ballast type (111) facet dominated morphologies on hotter edge and centre to (100) morphologies in intermediate (hotter) areas 37

Figure 39 - Raman of deposition on silicon substrate showing small Diamond peak at 1332 cm^{-1}. 37

Figure 40 - Comparison of (100) facets from run 16 (left) to run 18 (closed chamber run on right) confocal microscope images 50 × zoom 38

Figure 41 - Run 16, Raman of square faceted diamond sharp 1332 cm^{-1} peak (FWHM 4 cm^{-1}).. 38

Introduction

Significance of Diamond

In 1772, Antoine Lavoisier used sunlight, focused through lenses, to combust diamond. Comparing the quantity of carbon dioxide produced with that produced from the combustion of charcoal demonstrated that diamond was composed solely of carbon. This experiment opened doors to the field of diamond chemistry.[2] In the present day, properties of synthetic diamond including shape, conductivity and surface-chemistry can be modified, making it an advanced material.[3] Applications of synthetic diamond includes: wear-resistant cutting tools, electrochemistry, electronic devices and quantum technology. In electrochemistry and electronic devices, conductivity, therefore doping of diamond (with boron) is essential. However, in quantum technology, optical transparency and low defect density are the most significant properties.[3] The numerous applications of diamond create demand for high growth-rate synthesis methods, exhibiting high control over properties of the resultant diamond.

Diamond Properties

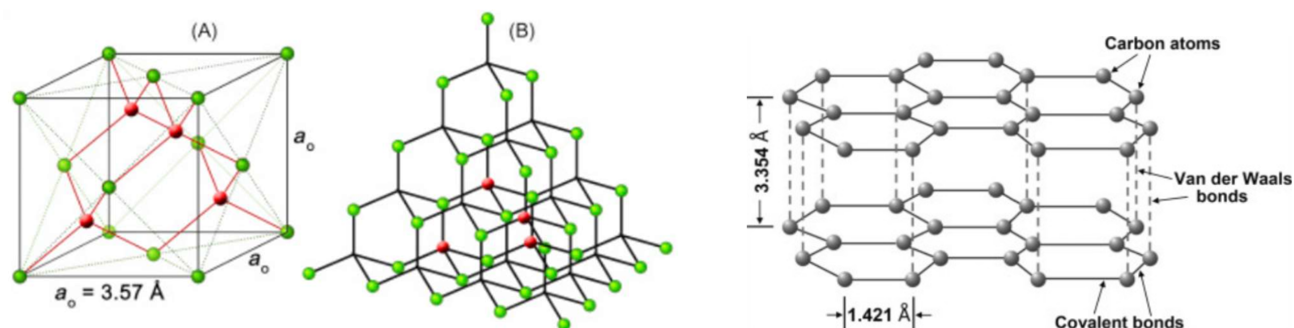

Figure 1 - The crystal structure of diamond by unit cell and lattice structure, bond length 3.57 Å, compared to graphite lattice structure, intralayer and interlayer bond lengths 1.42 Å and 3.35 Å respectively. Figure from Reference 1. [1]

Elemental carbon exists in allotropes, unique structural forms, whose abundance and properties vary. Diamond, Figure 1, is composed of sp^3 hybridised carbon atoms in a tetrahedral lattice. [4] The lattice gives rise to the most closely arranged atoms in any known structure with covalent bond length of 1.54 Å. [1] This gives diamond superior hardness and a single crystal thermal conductivity of 25 W cm^{-1} K^{-1}, more than six times that of copper. [4,5,6] Diamond is electrically insulative but can be made conductive by doping. [4,7]

In contrast graphite, Figure 1, is composed of sp^2 hybridised carbon in graphene sheets. Intralayer bonds are strong at 1.42 Å in length, compared to 3.35 Å between layers.[1] The weak inter-layer interactions are due to van-der-Waals forces, making graphite soft as layers are able to slide over each other.[8] In addition, graphite is naturally conductive without dopant due to the delocalised electrons between layers.[8] Graphite is the more thermodynamically stable allotrope, with a small difference in Gibbs free energy of 2.9 kJ mol^{-1}.[4] However, the Debye temperature for graphitisation of diamond is 1880 K, due to high activation energy of the conversion process, this value is heavily dependent on the crystal lattice size.[9] At temperatures

below the Debye temperature, diamond is stable, therefore the allotropes will not interconvert at room temperature.[10]

Diamond Synthesis

1.2.1 High Pressure, High Temperature (HPHT)

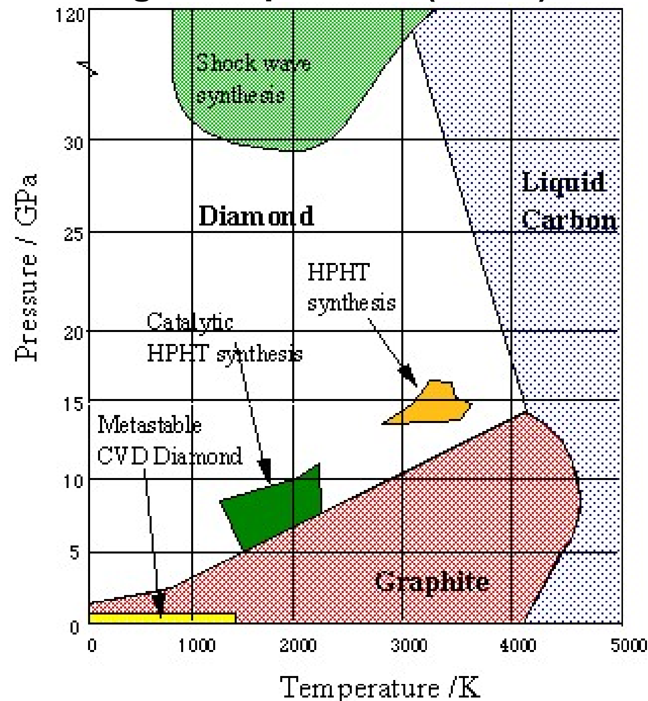

Figure 2 - The phase diagram of carbon stability showing pressure (GPa) against Temperature (K) where natural synthesis is shown at intermediate pressures and high temperatures whereas CVD diamond growth is low pressure low temperature. Figure from Reference 11. [11]

Figure 2 demonstrates that more conditions favour graphite formation over diamond. In nature, diamond is formed slowly under extreme pressures and temperatures, (4.5 - 6 GPa, 1500 °C), therefore initial attempts at man-made diamond were underlined by the same high-pressure, high-temperature principles.[12] The first successful synthetic diamond was produced in 1955 at 7 GPa and 1870 K.[12] Conditions were softer and had a higher growth rate than in nature, therefore were safer and more economical, this was due to a metallic solvent, in this case iron sulphide. [13] [12] The metallic solvent created a liquid flux, dissolving graphite thus increasing rate of diamond formation.[14]

HPHT has limitations including growth shape, as well as high energy demands. [5, 15] Furthermore, inherent to the method are the metal catalysts, which results in metal inclusions within the lattice.[14] Despite the low number density of inclusions, they produce internal stress, limiting application in tools as well as accuracy in electronics and sensors.[16]

CVD background

Chemical vapour deposition (CVD) is the utilisation of gas-phase chemical reactions to form solid deposits and has lower energy requirements than HPHT.[4] Diamond growth by CVD was first published by William G. Eversole in 1962, low-pressure CVD came later in 1968 by Angus. [17,18] CVD is advantageous in its ability to produce

diamonds of higher purity than both natural and HPHT diamonds, excellent for electrical applications. [19,20] Other CVD diamond applications include optical coatings, X-ray windows and wear-resistant films.[21]

CVD Growth Mechanism

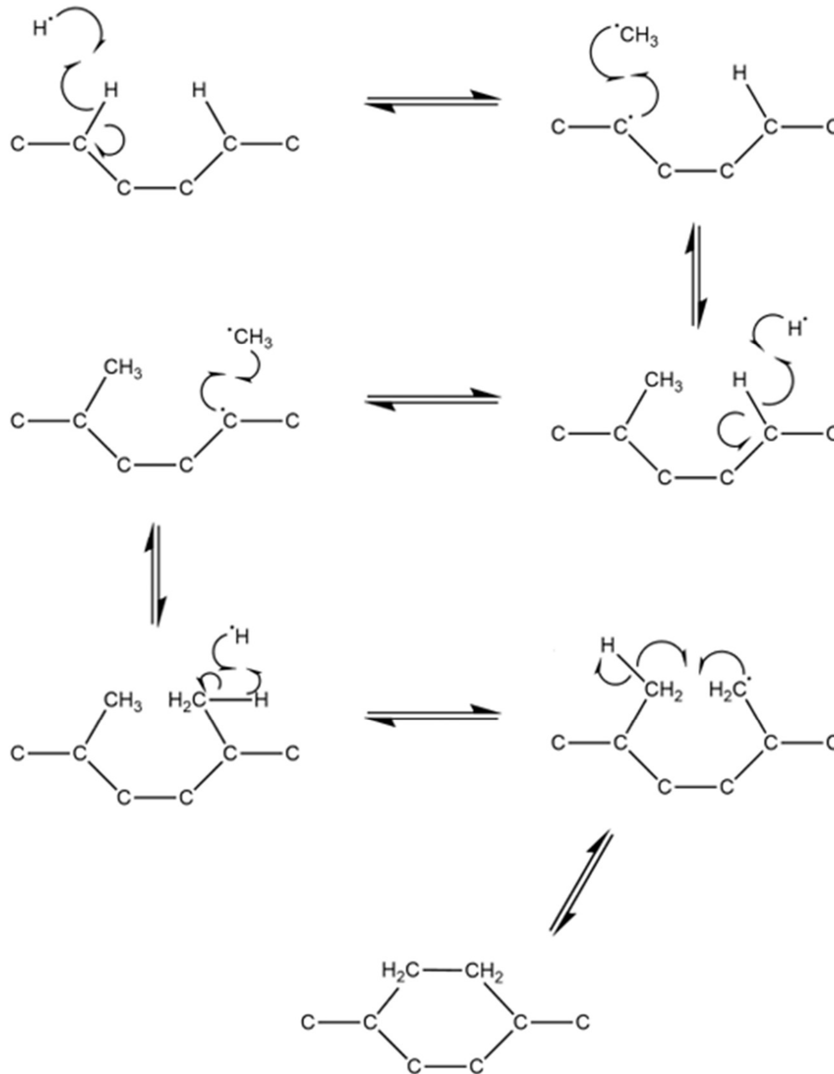

Figure 3 - The stepwise radical growth mechanism of CVD diamond. Figure from Reference 22. [22]

The stepwise growth mechanism, Figure 3, begins with H-atom abstraction from the surface using a H radical from the plasma, creating a reactive carbon on the surface. Due to the plasma composition being mostly H atoms, frequently the abstracted H radical will be replaced by another, causing no net change to the growth surface. On occasion, the exposed reactive site on the surface will meet a CH_3 radical; in this case, CH_3 adds on to the existing diamond surface, any of its three attached hydrogen atoms are now susceptible to the same H-atom abstraction described above. H-atom abstraction on a methyl group adjacent to another methyl group will result in a further C-C bond forming within the lattice.[4]

The role of hydrogen radicals within the growth mechanism is not just to propagate a further radical on carbon, they also etch sp^2 hybridised carbon at a faster rate than sp^3 hybridised carbon, removing any graphitic clusters formed on the substrate and improving the quality of diamond produced. [4]

Table 1 – Adapted from Angus et al, the key enthalpy (kcal mol^{-1}) and free energy (kcal mol^{-1}) of key gas-diamond and gas-substrate reactions during CVD diamond growth. Reactions 1 – 6 occur in the gas phase and 7 – 9 occur with the substrate (S). (1 kcal = 4.184 kJ) [17]

Reaction number	Reaction	Temperature / K	ΔH° / kcal mol^{-1}	ΔG° / kcal mol^{-1}
1	$H_2 \rightarrow 2H$	2500	+ 109	+ 37
2	$H + CH_4 \rightarrow CH_3 + H_2$	1800	ca. 0	- 11
3	$H + H + M \rightarrow H_2 + M$	1800	- 108	- 57
4	$CH_3 + H + M \rightarrow CH_4 + M$	1800	- 108	- 45
5	$CH_3 + CH_3 + M \rightarrow C_2H_6 + M$	1800	- 86	- 26
6	$C_2H_x + H \rightarrow C_2H_{x-1} + H_2$	1800	small	small
7	H + S → S—H	1200	- 94	- 68
8	S—H + H → S + H_2	1200	- 13	- 6
9	CH_3 + S → S—CH_3	1200	- 81	- 47

Commonly, CVD diamond will occur on an existing diamond substrate, homoepitaxially, in this case the mechanism in Figure 3 gives a full picture. However, if grown on a non-diamond substrate (heteroepitaxial), the nucleation step must be considered. This heteroepitaxial nucleation is slow because hydrogen in the plasma rapidly etches carbon deposits. Bias Enhanced Nucleation (BEN), increases nucleation density by applying a voltage to the substrate, increasing ion bombardment.[4] Equations 7, 8 and 9 in Table 1 describe the substrate radical interactions.

The growth of individual diamond crystals is accounted for by the stepwise mechanism; however a polycrystalline film requires the meeting of many separate crystals. When the nuclei meet to create a continuous film the chemistry is less well known, specifically relating to the rate of CH_2 bridge species. This is the first of two research gaps. The second of which being the role of C_2, which although not involved in the growth mechanism could be significant in defect formation or renucleation. [23]

Gas ratio for growth

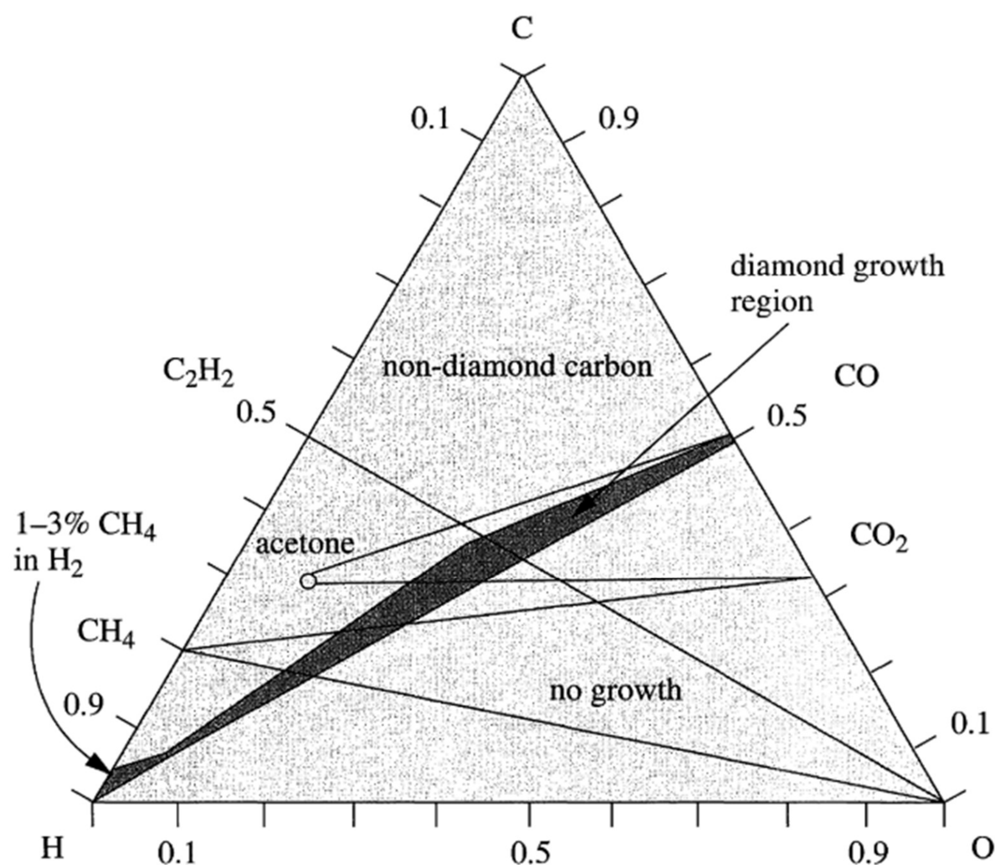

Figure 4 - The Bachmann triangle of diamond growth. Most CVD occurs with only CH_4 and H_2 at 1 - 3 % methane.[4]

Conditions where diamond is metastable relative to graphite are narrow, Figure 4.[17] This region is called the diamond domain and is applicable to all CVD methods.[24] Bachmann noted limitations in this diagram expressing the need for a third dimension: temperature.[24] The small region in the bottom left (1 – 3 % methane) accounts for almost all CVD growth proccesses.[4] However, CVD at higher methane concentrations is frequently performed, compromising film quality for a higher growth rate as the relative concentration of H (to etch sp^2 deposits) is decreased.[4]

Methods of radical activation

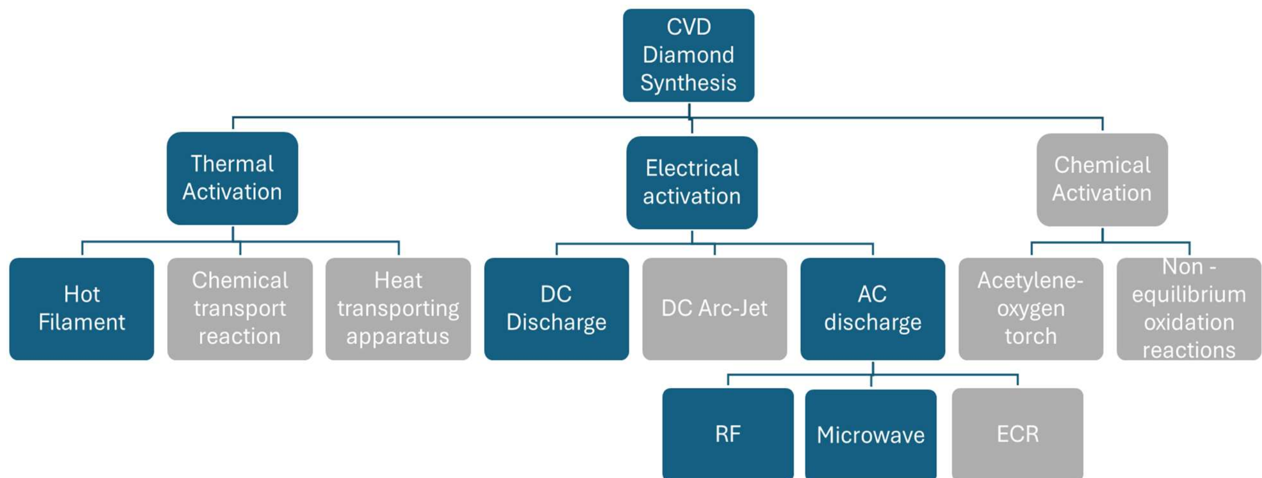

Figure 5 - Adapted from Reference 5, categorisation of radical activation techniques used for CVD diamond growth, with those performed in Bristol Diamond Laboratory highlighted in blue.[5]

Techniques for radical initiation in CVD can be categorised into: thermal, electrical and chemical activation types.[5] Photochemical activation is also possible, however, is only occasionally used, exclusively within hybrid techniques, therefore it has been excluded from Figure 5. [5]

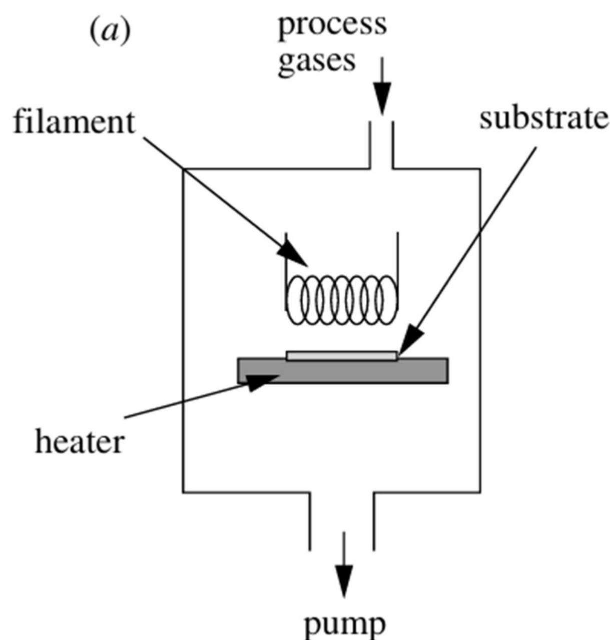

Figure 6 - An exemplar hot filament CVD reactor from Reference 4.[4]

A hot filament CVD reactor is shown in Figure 6. The filament is heated to 2200 °C, sufficient to ionise the low pressure (20–30 Torr) gas mixture within the chamber. This leads to polycrystalline film deposition on the substrate, heated to 700 °C. Hot filament CVD is limited by filament durability at such high temperatures, with oxidation or corrosion by gases leading to metal inclusions, deeming deposited film unsuitable for electronic applications.[4]

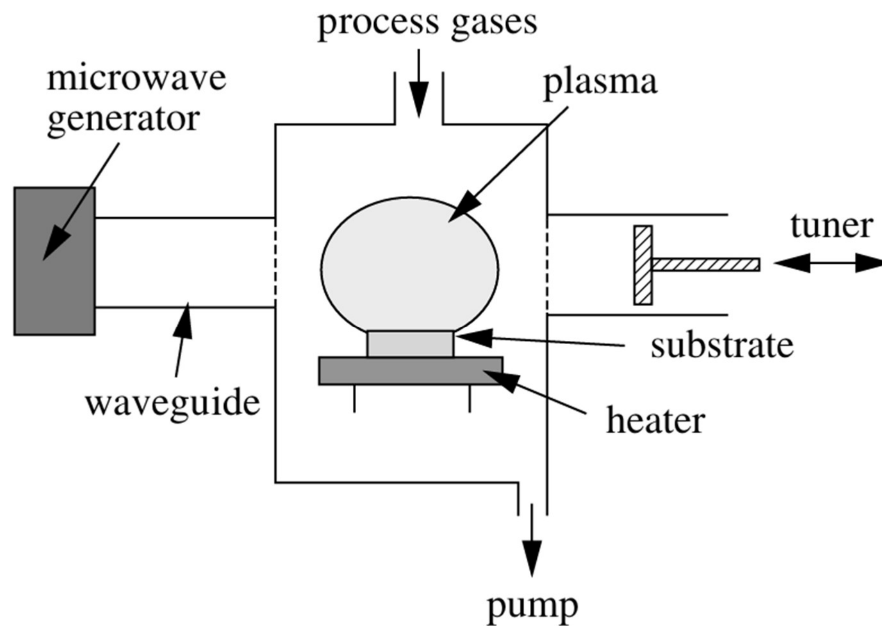

Figure 7 – A diagram of a Microwave CVD reactor from Reference 4.[4]

Microwave CVD, Figure 7, utilises microwaves (frequency 2.45 GHz) which transfer energy to gas phase electrons, in turn increasing frequency and energy transfer of collisions, therefore heating the gas mixture and causing ionisation.[25] The reactor is more expensive than hot filament, yet solves the problem of metal inclusions.[4] This technique is often coupled with bias-enhanced nucleation (BEN) for heteroepitaxial growth to plant carbon within the substrate surface layers.[4] BEN adds complexity to the reactor, increasing cost of an already expensive reactor.[4]

Direct Current (DC) CVD

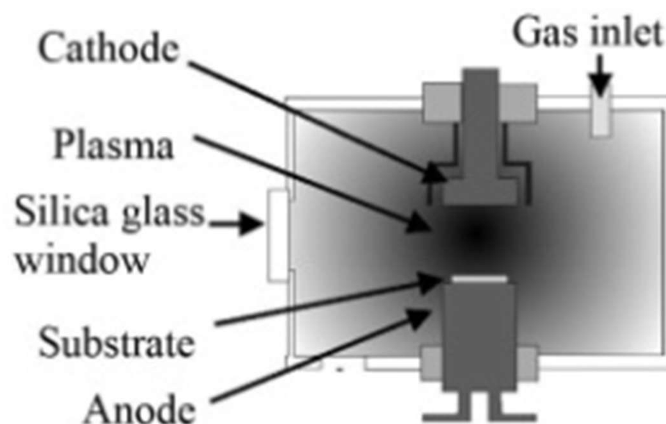

Figure 8 - Figure of simplified DC CVD reactor taken from reference 5. [5]

DC CVD, Figure 8, is advantageous as the voltage applied both biases the substrate and activates the plasma, simplifying the reactor setup. Additionally no substrate pre-treatment is needed for growth in DC CVD, as opposed in other techniques which typically need seeding if BEN is not used.[26]

The DC reactor, Figure 8, operates under a high voltage applied to the cathode, to initiate an avalanche breakdown. In an avalanche breakdown the cathode emits high-energy electrons. The liberated electrons travel until they collide with a gas-phase molecule. Upon collision the impacted molecule will absorb the high energy electron it has been impacted by and in turn release an electron, continuing the movement of charge. Many electrons are accelerated upon release due to repulsion by the cathode and attraction to the anode, but, as direction of the liberated electron is random, sometimes the converse is true. The energy of impacting electrons is less than the electrons released as a result of collision, therefore the voltage required to create a discharge increases with both increasing electrode gap and increasing pressure. Pressure impacts the mean free path, meaning the average distance an electron or ion can travel before impacting. This electron transfer process is called electron impact dissociation and will produce radicals seen in growth mechanism.[27] The plasma is struck in a hydrogen atmosphere as hydrogen has lower electron impact dissociation enthalpy than methane, which is added later.[22, 28]

$$V_b = \frac{Bpd}{\ln(Apd) - \ln\left[\ln\left(1 + \frac{1}{\gamma_{se}}\right)\right]} \qquad (1)$$

$$A = \frac{\sigma}{K_B * T} \qquad (2)$$

$$B = \frac{\varepsilon_i * \sigma}{e_c * K_B * T} \qquad (3)$$

Voltage breakdown required for radical formation occurs according to Paschen's law, Equation 1, where A and B are constants, p is pressure, d is plate separation and γ_{se} is the secondary electron coefficient at the cathode. Constant B is found from ε_i ionisation potential, σ ionisation cross section as well as e_c elementary charge K_B Boltzmann's constant and T temperature. This gives further detail to the non-linear relationship of breakdown voltage to both pressure and plate separation.[29]

Qualitative characteristics of a DC glow discharge

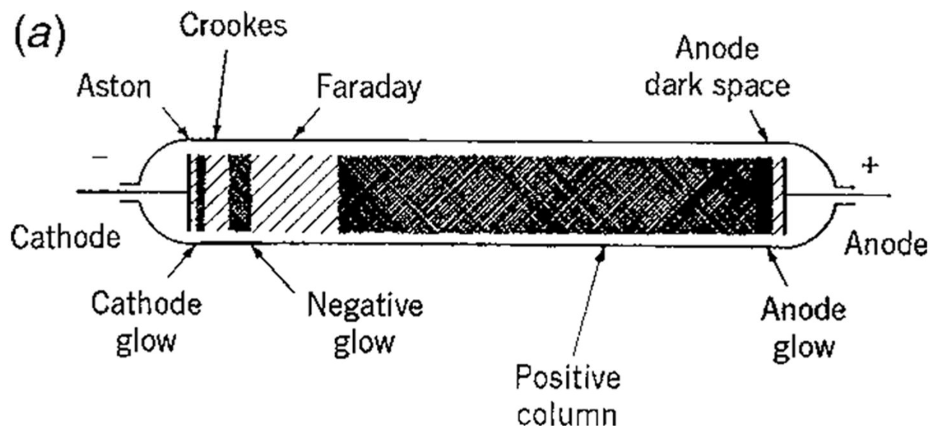

Figure 9 - Characteristics of a glow DC discharge from cathode to anode. From reference 30 (chapter 14) [30]

Properties of a DC glow discharge vary from cathode to anode, Figure 9. The cathode glow is a result of high-velocity electrons from the electric field. The Crookes dark space is as result of the exclusion of electrons from the positive column, leaving only large ions to carry charge and causing a large fall in voltage across this region. In the Faraday dark space electrons from the positive column are decelerated by the cathode then reaccelerated. The reaccelerated electrons have too low energy for electron impact dissociation, therefore, there is no glow in the Faraday dark space. The positive column is quasi-neutral, containing electrons and ions. The electrons partake in electron impact dissociation and excitation, subsequent de-excitation of ions through radiative pathways gives the characteristic ‘plasma glow’. At the anode there is a double layer where thermal electrons reach the anode first and create a double layer, slightly repelling further electrons, causing a small drop in voltage. The anode itself is still positive and the implications of this double layer on plasma dynamics are minimal.[30]

Pulsed DC CVD

In traditional DC CVD methods, power, area and duration are limited, if any of these parameters are increased too much the glow discharge collapsed into an arc discharge.[27] Two solutions were proposed: Firstly, magnetic field discharge stabilisation, proposed by Nesladek, achieved a substrate diameter of 3.5 cm. Alternatively, a pulsing of the power supply, proposed by Hartmann. [27, 31] Use of a pulsed DC current was successful for Hartmann, strictly limited by pulse to pause ratio not causing cathode temperature to exceed 1000 °C. Additionally, Hartmann found that pulses should be longer for higher methane concentrations and lower power densities. [27]

A benefit of pulsed DC compared to DC discharge is a much higher plasma density therefore increase in ionisation of growth species. Lundin and Sarakinos suggested electron density in the plasma increases from 10^{17} m^{-3} to 10^{19} m^{3} by pulsing the DC current. This resulted in a mean free path decrease from 50 cm to 1 cm, advantageous for film quality.[32] Therefore pulsed magnetic field discharge stabilisation. However, pulsed DC is more likely to melt the substrate or cathode, due to higher maximum power, therefore pulse time in duty cycle must be kept low to prevent cathode melting.[33]

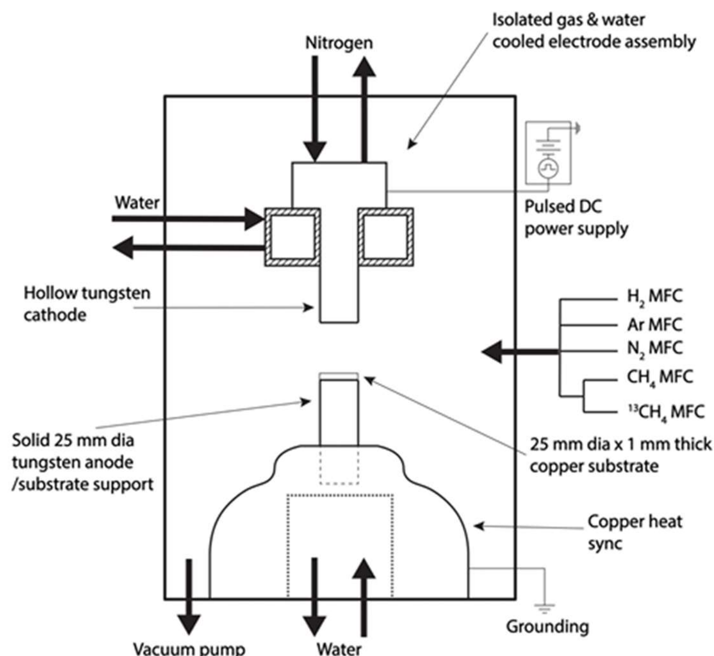

Figure 10 - A diagram of the pulsed-DC reactor present in the Bristol Diamond Laboratory built by Palubiski from Reference 22 [22]

The design of Hartmann's pulsed DC reactor formed the basis of the pulsed DC reactor in University of Bristol school of Chemistry built by Dominic Palbuski in 2016, Figure 10.[22]

Considering Substrates for Pulsed DC CVD

Often in heteroepitaxial growth substrates are seeded to increase nucleation density by depositing small diamond crystals which need only lateral growth not nucleation to form a diamond film [21] However Lee et al proved that this process did not leave diamond on substrate in DC CVD as the initial hydrogen plasma etched these 'seeds'.[34] It was therefore concluded that due to the necessary hydrogen plasma of DC CVD seeding would not be effective therefore substrate properties were crucial.[34, 23]

Substrate type can be broadly categorised by its solubility to carbon. Type 1 has low solubility to carbon, exemplified by copper. Type 1 does not from a carbide layer therefore is excellent for free standing films but suffers from delamination.[4] Type 2 films have strong carbon solubility but weak carbide formation, therefore early in growth carbon diffuses into the bulk, this delays nucleation. Type 3 have a strong carbide layer formation resulting in strong film-substrate adhesion examples of such substrate materials include Mo or Si. Films deposited on type 3 substrates exhibit the highest stress due to strong adhesion coupled with thermal mismatch, this results in Raman shift differing from expected 1332 cm^{-1}.[35]

Considerations aside form carbide layer formation include thermal expansion coefficient, melting point and electrical conductivity - a requirement unique to electrical radical activation methods.[22, 23]

This project focused on the use of two substrate materials, molybdenum and silicon. Molybdenum has a lattice constant close to that of diamond, good for heteroepitaxial deposition, as well as a high melting point of 2622 °C. It is type 3 so forms a Mo_2C film at 700 - 770 °C.[36] Silicon has a very similar thermal expansion coefficient to diamond and forms primarily SiC as a carbide layer.[36] Silicon is a more challenging substrate than Molybdenum as it is electrically insulating and has a low melting point of 1411 °C.[37, 38] One method to navigate this is near-plasma DC CVD where the silicon substrate is adjacent to the plasma but not seated on the anode, however this still required BEN.[37] Silicon can be doped with boron to make a p-type semiconductor, navigating electrical conductivity problems.[39] Growth on silicon substrates is desirable due to its acid solubility which can be utilised in the creation of free standing diamond wafers.[40]

Literature Results from Pulsed DC CVD

The sensitivity of pulse to pause ratio in pulsed DC CVD was emphasised by Hartmann where 72 μs/ 50 μs facilitated diamond growth whereas 75 μs/ 50 μs resulted in uncontrollable plasma rotation, both at 5 % methane. Hartmann achieved growth on a circular substrate, 3 cm in diameter at growth rate 40 μm h^{-1} and methane concentration 4 %.[36] Hartmann also found that 4 % methane concentrations relative to hydrogen was best for deposition, considering diamond growth rate and film quality across facet centre and grain boundary.[27]

The highest area depositions reported in literature were 70 cm^2, however this was at a very low pressure of 40 Torr, therefore a very low growth rate, less than 0.1 μm h^{-1}. At a higher pressure, 150 Torr, deposition rates were able to achieve 20 – 250 μm h^{-1} however, the maximum area for such rates was 2 cm^2. [27]

Several studies conducted in the Bristol Diamond Laboratory have focused on optimisation of the pulsed-DC CVD reactor used in this study. In many runs, growth time was limited by plasma stability, the maximum growth time was 3.5 hours achieved by Harris, with occasional arcing throughout and terminated due to large arc. Arcing has been cited as a result-limiting problem in all studies using this reactor since its creation in 2016. Despite arcing, previous studies have shown deposition on tungsten, copper, molybdenum and iridium substrates, with the best continuous films grown on copper. Palubiski commented on lack of successful growth on silicon in this reactor stating that pulsed DC-CVD reactors are by design unsuited for silicon growth due to low conductivity, even when p-type silicon was used. Silicon caused difficulty striking plasma and tended to melt when instabilities arose, it was noted that all successful diamond growth on silicon in literature using pulsed DC CVD used a larger electrode area than substrate.[22]

Successful diamond deposition under closed chamber conditions has also been achieved in this reactor with little to no difference in morphology - mostly triangular (111) facets for highest film quality on 12.5 mm radius disks 3 mm thick.[22] Modifications to the reactor were made between the first and the last studies reviewed above include but are not limited to: electrode cooling system, electrode material, electrode area and power supply. For these reasons, conditions cannot be assumed to be transferable from previous studies and new conditions were required for this project.

Isotopically pure diamond

Carbon exists in three main isotopes ^{12}C ^{13}C are stable isotopes with natural abundances of 98.89 % and 1.11 %, respectively.[41] ^{14}C is radioactive with half-life of 5700 years and present in trace amounts. Use of monoisotopic, with respect to carbon, CH_4 in CVD has grown monoisotopic diamond. The isotopically pure ^{14}C methane is often sources from recycled nuclear waste, making sustainability. [5,14] Isotopically pure CH_4 is expensive, therefore CVD of isotopically pure diamond is best carried out under 'closed chamber' growth conditions, as opposed to under the continuous flow of growth gases. [42]

Beta Voltaic Diamond 'Batteries'

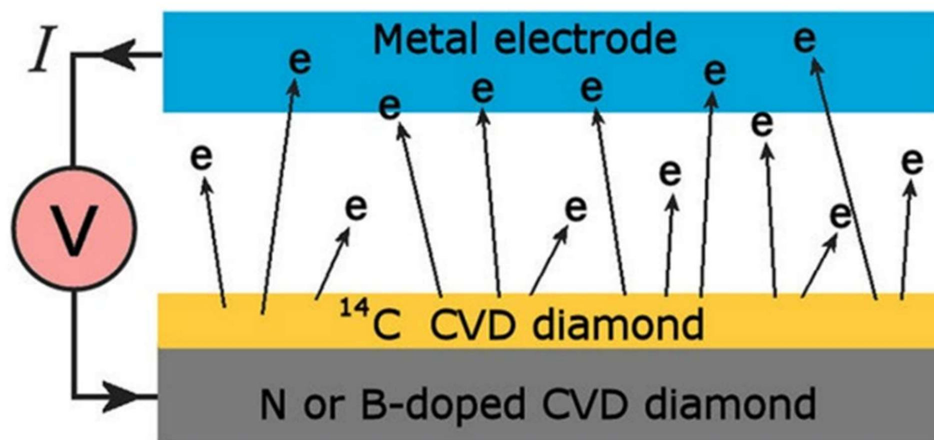

Figure 11 - A schematic of a beta voltaic diamond 'battery', demonstrating the emission of beta electrons by ^{14}C diamond creating the current. Figure from reference 3. [3]

Isotopically pure ^{14}C diamond can be used to produce an 'everlasting battery', Figure 11. This will generate a continuous flow of beta emitters, giving low power in the order of μW, for thousands of years. In the beta voltaic battery, Figure 11, the metal electrode acts as a 'collector electrode' with a 100 μm gap between metal and diamond electrodes. The battery is in a vacuum as to allow the beta electrons emitted by diamond to travel across the gap and strike the metal, causing a current to flow back to the emitter.[3]

Low power diamond 'batteries' have two primary applications: Firstly, the use of a trickle-charge capacitor would allow intermittent high-power for applications such as military surveillance or aerospace communication and sensors. Secondly the continuous low power can be harnessed in applications such powering smart devices for 'the internet of things' which have low, yet continuous power requirements.[3]

Project Aims

Pulsed DC CVD has been shown in literature to be beneficial in its ability to deposit diamond films, at high growth rates, over large areas.[22] The pulsed DC CVD reactor in the University of Bristol Diamond Laboratory has been limited by plasma collapse into an arc discharge (arcing) in every study conducted on the reactor since its inception in 2016.[22, 43, 44] The arcing has caused substrate melting and film destruction.[22] The absence of reliably stable plasmas limits the reactors applications as use of expensive substrates such as Iridium or feedstock gases such as $^{13}CH_4$ is expensive and wasteful if reactor behaviour is unpredictable. Changes to the electrode cooling system of the reactor required new operating conditions to be found. This study primarily aimed to understand factors contributing to plasma instability and in doing so produce diamond growth with reproducibly stable plasmas under new operating conditions.

Secondary and tertiary aims in this project were to achieve diamond growth on silicon and to measure the band gap of isotopically pure diamond on a single crystal diamond substrate grown in this reactor. Growth on silicon would prevent the delamination problems previously exhibited by copper substrates in this reactor, as it forms a carbide layer.[4, 22] Additionally, silicon can be dissolved chemically allowing free standing wafer production.[40] Isotopically pure diamond has applications in beta voltaic devices; in order to achieve this the reactor would need to be optimised for closed chamber growth runs.[3] DC CVD's aptitude for large area deposition would make it an excellent reactor for the production of isotopically pure diamond wafers.[22]

Experimental Methods

Theory of Spectroscopic and Characterisation Techniques

Optical Emissions Spectroscopy

Table 2 – The electronic transitions of species in a H_2/ CH_4 plasma and their characteristic fluorescence wavelengths from reference 43 .[45]

Excited species	Electronic transition	Peak position / nm
CH	$A^2\Delta \rightarrow X^2\Pi$	431.15
H_γ	$n' = 5 \rightarrow n = 2$	436.85
C_2	$d^3\Pi_g \rightarrow a^3\Pi_u$	471.55
H_β	$n' = 4 \rightarrow n = 2$	486.31
C_2	$d^3\Pi_g \rightarrow a^3\Pi_u$	516.52
C_2	$d^3\Pi_g \rightarrow a^3\Pi_u$	563.25
H_2	$3p^3\Sigma_u \rightarrow 2s^3\Sigma_g$	602.16
C_2	$d^3\Pi_g \rightarrow a^3\Pi_u$	619.12
H_α	$n' = 3 \rightarrow n = 2$	656.81

Optical Emission Spectrometry (OES) was used to analyse the wavelengths light emitted by the plasma. When radicals de-excite to the ground (X) state they fluoresce at a characteristic wavelength. Table 2 contains the key radical de-excitation pathways in a CH_4/H_2 plasma and the corresponding wavelengths.[45] The CH_3 radical is not in Table 2 as its excited state rapidly predissociates, therefore does not fluoresce.[46] Correlation of CH_3 to CH therefore C_2 radicals has been proven to be near-linear.[47] Additionally, the intensity of the C_2 peak in OES has a near linear correlation with the C_2 density in the plasma. These factors make C_2 emission intensity a suitable parameter to estimate density of CH_3 growth species density.[47] OES is especially beneficial as it has no effect on the plasma dynamics yet measures reactive species and excitation.[45] The strong CH and C_2 growth species correlation have been proven, validating the use of C_2 to discuss the presence of growth species CH.[47]

Confocal Laser Microscopy

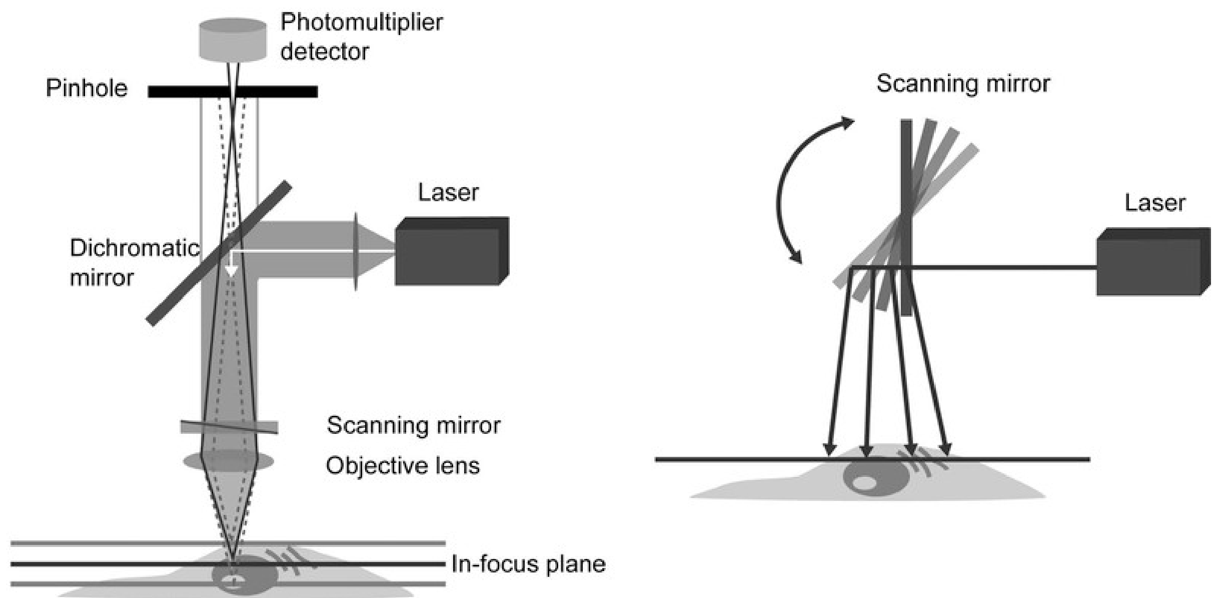

Figure 12 - Confocal laser spectroscopy technique, using a scanning mirror and dichromatic mirror to focus laser onto a single plane of the sample. Figure from Reference 46.[48]

Confocal laser microscopy allowed 3D constructions of the film analysing the sample in planes and rejecting out of focus light. This gave high resolution images with low noise. Figure 12 depicts the use of laser on both a dichromatic mirror, to focus the beam on a single point, and a scanning mirror to move across the sample point by point and the detection of reflected light by the photomultiplier device. The best resolution which can be achieved by confocal laser microscope is 0.2 μm laterally and 0.6 μm axially. This resolution is substantially higher than regular light microscopes, where resolution is determined by the numerical aperture of the objective lens.[48] In the Bristol Diamond Laboratory a Laser scanning confocal microscope is in place, used to determine film morphology and thickness.

Scanning Electron Microscopy (SEM)

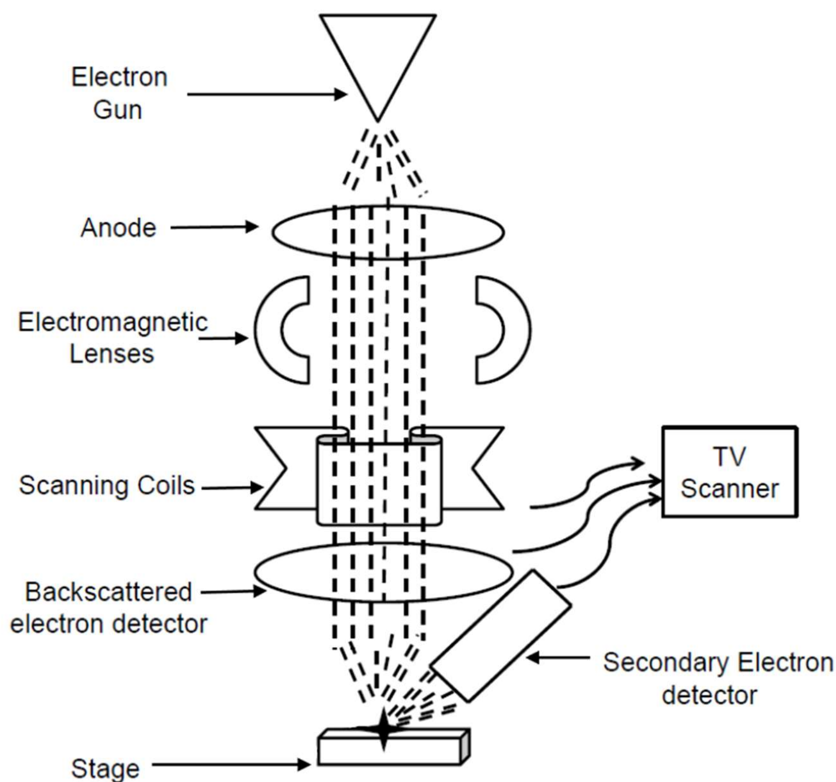

Figure 13 - Diagram of an SEM demonstrating acceleration of electron beam by anode, focusing by electromagnetic coils and detection of backscattered and secondary electrons. Figure adapted from reference 47.[49]

Scanning electron microscopy (SEM), Figure 13, is useful for higher-resolution descriptions of film morphology, compared to confocal laser microscopy. The resolution is significantly higher, as a single electron beam is scattered from the surface and depicting surface texture as well as conductivity, as opposed to higher wavelength photons.[36]

Raman Spectroscopy

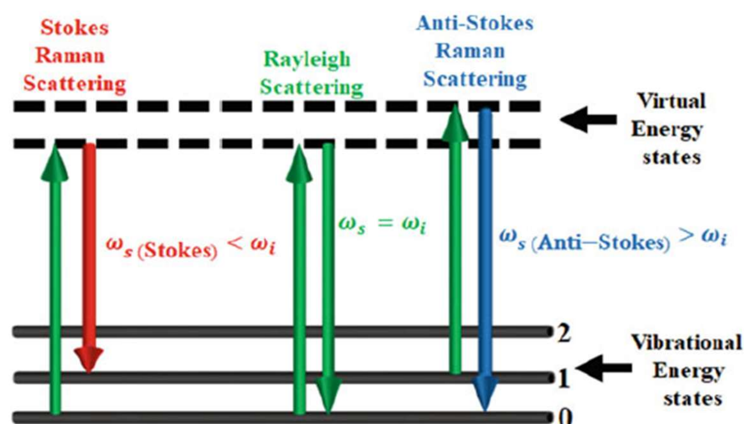

Figure 14 - The interaction between vibrational energy levels of a material and monochromatic incident photons either through Raman or Rayleigh scattering. Figure from reference 48 .[50]

Raman scattering occurs when vibrational energy levels of a material either decrease the energy of the incident photon levels (Stokes) or add energy to the incident photon (Anti-Stokes). These are the exception, Rayleigh scattering is the dominant process, whereby the incident scattered photons have equal energy, therefore scattering is elastic.[50] Figure 14 depicts Raman and Rayleigh Scattering.[50]

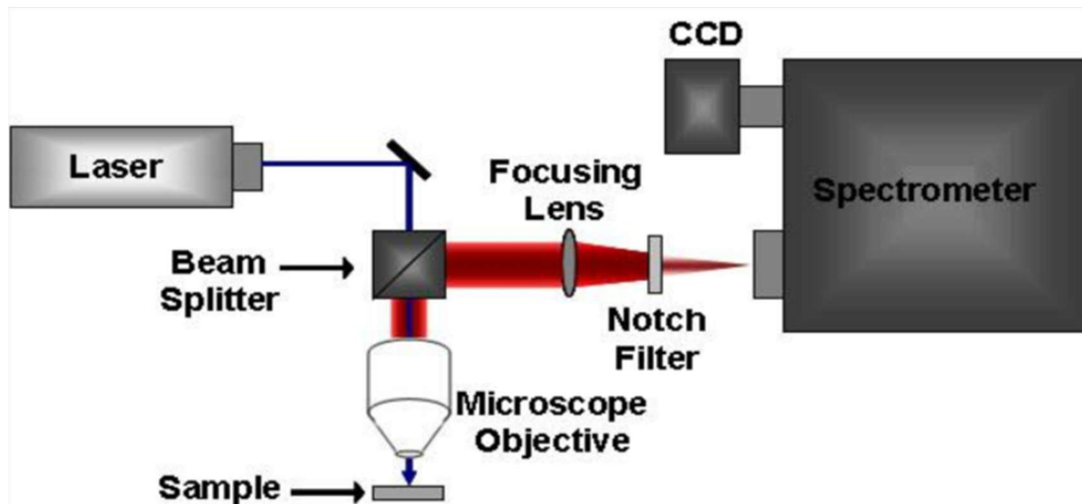

Figure 15 – An Exemplar Raman Spectrometer where a Charge-Coupled Device (CCD) captures digital spectra. Figure adapted from Reference 49. [51]

Diamond can be characterised by its unique Raman scattering in a Raman spectrometer, Figure 15. When a light source in the form of a laser is directed at a sample most scattering occurs at the same wavelength, elastically, this is Rayleigh scattering; however, some is scattered at a different wavelength, Raman scattering.[52] A peak at 1332 cm^{-1} is characteristic of diamond, whereas 1550 cm^{-1} is non-diamond carbon impurities which are sp^2 hybridised such as graphite and amorphous carbon.[6] The reliability of Raman peak intensity to abundances of non-diamond impurities is very poor, due impurities absorbing very strongly in the visible region and exhibiting Raman scattering efficiency 50 times higher than that of diamond. [6]

The Pulsed DC CVD Reactor

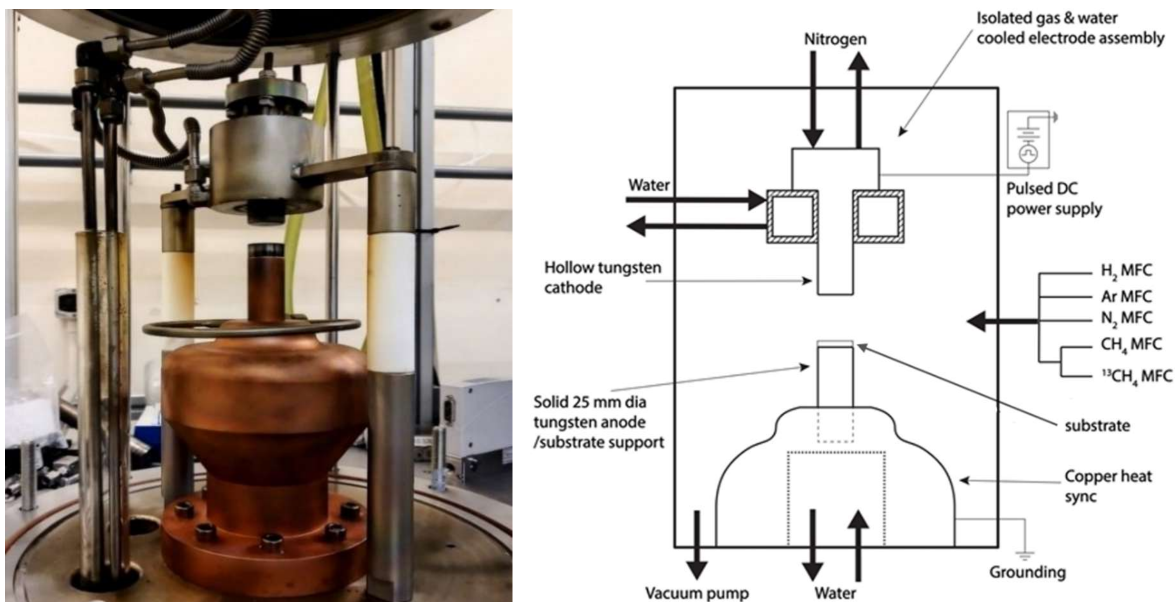

Figure 16 - On the left, inside the chamber of the pulsed DC CVD reactor present in Bristol Diamond Laboratory showing the copper cooling jacket surrounding the anode along with the gas ring and cathode. On the right a diagram of the same reactor adapted from Reference 22 .[22]

Figure 17 - The pulsed DC CVD reactor in the Bristol Diamond Laboratory, nicknamed ‘The Minion’. The dome shaped growth chamber and computer used to run LabView and visible.

The pulsed-DC PA-CVD reactor in the Bristol Diamond Laboratories, Figures 16 and 17, was built in 2016 by Dr James Smith and D. Palubiski based on Hartmann’s design. A steel dome, with chamber volume of 15 L supported internal pressures of below 0.01 Torr. Tungsten electrodes, 12.5 mm diameter, were water-cooled, water temperature 17 – 21 °C with electrode gap variable between 5 – 25 mm. Further cooling was provided to the anode by a copper heat sink. An Advanced Energy Pinnacle Plus+ Pulsed-DC power supply was connected to the cathode, with a maximum power of 10

kW; although working maximum has been approximated at 2.5 kW due to the electrode cooling system.[43] The anode was grounded relative to the cathode. Feedstock gas flow rates were controlled by Burkert mass flow controllers (MFCs), one for each of H_2, CH_4, $^{13}CH_4$ and Ar. Gases entered the chamber from MFCs through a perforated gas ring (perforations spaced at 1 cm intervals with diameter 2 mm) positioned below the anode. Outflow to the pump was controlled by a butterfly valve via a MKS vacuum controller.

This project included two modifications made to the reactor under the direction of Dr James Smith. Firstly, Burket MFCs were replaced by newer Burket MFCs with increased hydrogen flow capacity from 500 to 1000 sccm, calibration and leak testing of the new MFCs was performed, detailed in appendix. Secondly, to prevent computational time-out, a copper-mesh screen was installed. The screen separated high and low voltage wiring. This facilitated change in scale down procedure from manual, used in runs 1 – 6, to computational, used in runs 7 – 19.

Growth Procedure

Laser Cutter

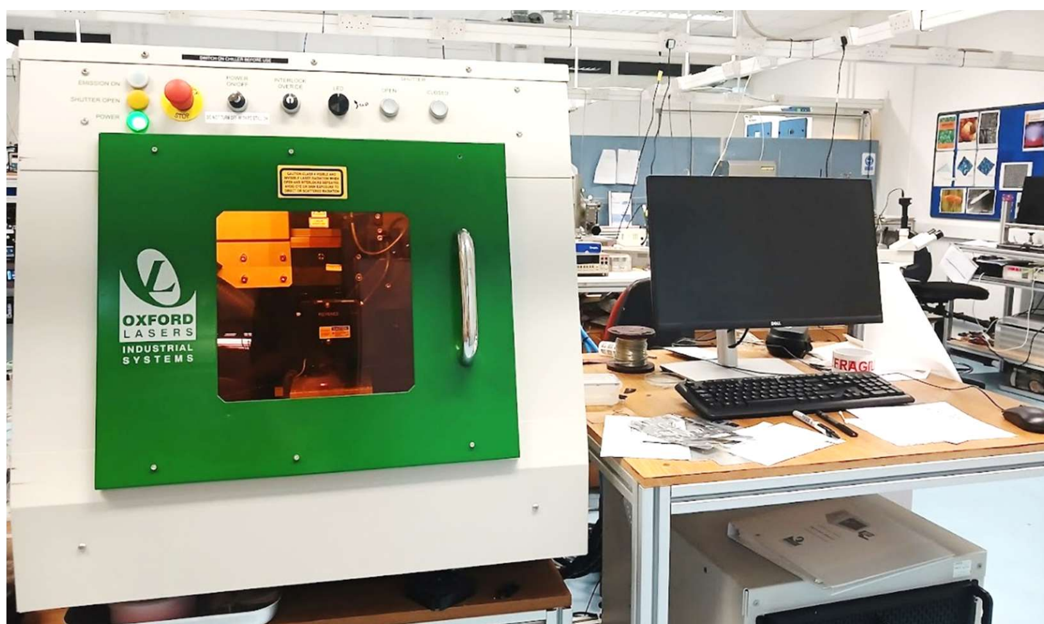

Figure 18 - Image of Oxford Lasers, laser cutter system present in the Bristol Diamond Laboratory.

Circular molybdenum and silicon (boron doped, Resistivity 10^{-3} - 40 Ω cm) substrates of 25 mm diameter and 0.5 mm thickness were laser cut with the Oxford Laser system, Figure 18. Alphacam3 software was used to design cut path. Two annuli 0.5 mm thickness with cutouts of 5 mm and 10 mm radius respectively were produced, from an Mo sheet to function as a thermal break between anode and substrate. Two further MO thermal breaks were cut with spiral grooves and a linear cut across with 40 % and 15 % area missing respectively, this prevented trapped volume.

Reactor Operating Procedure

This procedure was adapted from 'The Minion SOP' document.

Start-up

The reactor was kept under vacuum below 0.02 Torr when not in use. An argon purge was conducted up to 745 Torr, subsequently chamber was opened, substrate and thermal break (if used) were loaded ensuring even placement on anode. Chamber was closed, butterfly valve to pump was opened. The chamber was evacuated to pressures below 0.02 Torr. The reactor was left in this state, often overnight. To begin growth, water flow to cool electrodes was begun. Using LabView hydrogen flow rate was set to 500 sccm and target chamber pressure was set to 100 Torr. Plasma was struck at 50 W, 125 Hz, pulse rest time 2.5 µs, and chamber pressure 2.5 Torr. Power was increased to accommodate increasing hydrogen pressure at 10 W: 1 Torr. At 100 Torr methane at flow rate 20 sccm was added, 3.8 % methane concentration in the gas mixture and target pressure, between 165- 185 Torr, was set. Scale up continued at ratio 10 V to 1 Torr until pressure reached target pressure, final power was set.

In-run procedure(s)

The power and pulse rest time were altered. At 60 minutes rest time of duty cycle was either changed or maintained. A growth run was deemed to have 'started' once the second target pressure had been achieved, run durations of up to 4 hours were conducted. In the closed chamber run continuous flow occurred for 100 minutes then, simultaneously MFC flow rate was set to zero and butterfly valve to pump was closed to maintain chamber pressure. At 125 minutes and 150 minutes a 1-minute CH_4 injection, flow rate 20 sccm, was added to maintain optimal CH_4 concentration for growth rate. If used, a Broadcom Qmini spectrometer was directed at the centre of the plasma and acquisitions taken at 10-minute intervals. Acquired spectra were analysed in Waves software. After target run duration was met, scale-down procedure 1 or 2 was followed.

Scale down procedure 1 – Manual control

LabVIEW program was shut, this caused pneumatic valves to hydrogen and methane MFCs to close, simultaneously the butterfly valve to the pump was closed. Intermittently for durations of 2 seconds the valve to the pump was opened and pressure decreased by approximately 10 Torr per opening. For each 10 Torr power decrease power was decreased by 100 Watts. Once the plasma was extinguished, power and power supply were turned off. Chamber was evacuated and remained under vacuum to allow substrate cooling. The butterfly valve to the pump was closed and argon was used to purge chamber to 745 Torr, the chamber was opened and the substrate was retrieved.

Scale down procedure 2 – Computational control

After the run duration the flow rate of the methane MFC was set to 0 and valves were closed. A hydrogen flush was carried out for 10 minutes, with hydrogen flow rate 500 sccm and no methane flow, pressure consistent with that used during the run. This gradually decreased partial pressure of methane within the chamber,

creating a hydrogen plasma which etched sp^2 hybridised carbon, therefore increased film quality. The power was scaled down linearly over 3 minutes. As soon as plasma was extinguished the power and power supply were turned off and chamber was evacuated. The chamber was left under vacuum (0.2 Torr) for the substrate to cool. The butterfly valve to the pump was closed and argon was used to purge chamber to 745 Torr, the chamber was opened and the substrate was retrieved.

Analytical Methods

All samples were analysed using the Confocal Laser Microscope, LEXT OLS5100. The 3D scan feature was used to assess film thickness. Analysis using Raman system microscope Renishaw SM2000 was used at laser power 33 % and wavelength 514 nm with centre 1332 cm^{-1} was carried out. Films produced by growths 17, 18 and 19 were analysed using SEM under the supervision of Dr Liam Cullingford.

Summary of Growth Conditions

Table 3 – A summary of the growth conditions (power, rest time, pressure, duration, thermal break and electrode gap) used in each run.

Run	Power / W	Rest Time / µs	Starting Pressure / Torr	Duration / minutes	Thermal Break	Electrode gap / mm
1 – F = 100kHz	1740	2.5	173	60	No	17
2	1740	2.5	174	60	No	16
3	1820	2.5	181	60	No	16
4	1810	2.5	180	60	No	16
5	1800	2.5	176	90	No	16
6	1790	2.5	175	75	Mo disk	15.5
7	1800	2.5	No result	-	A	15.5
8	1800	2.5	170	75	A	15.5
9	2000	2.5	170	150	B	15.5
10	2000	2.5	No result	-	A	15.5
11	2000	2.5	170	70	A	15.5
12	2000	2.5	170	90	D	15.5
13	2000	2.5	170	90	C	15.5
14	1800	2.5	180	90	C	15.5
15	1650 - 2200	Varied 3.0 to 1.2	165	60	C	15.5
16	1750	2.0	170	240	C	15.5
17	1750 - 1800	2.5 then 1.6	170	180	C	15.5
18*	1751 - 1800	2.5 then 1.2	170	180	C	15.5
19**	1750	2.5 then 3.0	170	150	C	15.5

*Closed chamber growth
**Growth on a silicon substrate

Results and Discussion

Previous studies on this reactor used Taguchi optimisation, these reports noted the limited usefulness of such optimisation, as plasma stability governed results. In A. Billings' Taguchi array, 5 out of 16 growth runs were not terminated by arcing therefore produced useable results.[43] This report used iterative optimisation and aimed to achieve conditions for stable plasma before optimisation for deposition quality.

Optimisation for Plasma Stability

An Unstable Plasma (Run 3)

Figure 19 – On the left a plasma arc resulting from a 2° misalignment between electrodes Power: 1810 W Pressure: 180 Torr and resulting deposition on a 25 mm Mo substrate on the right.

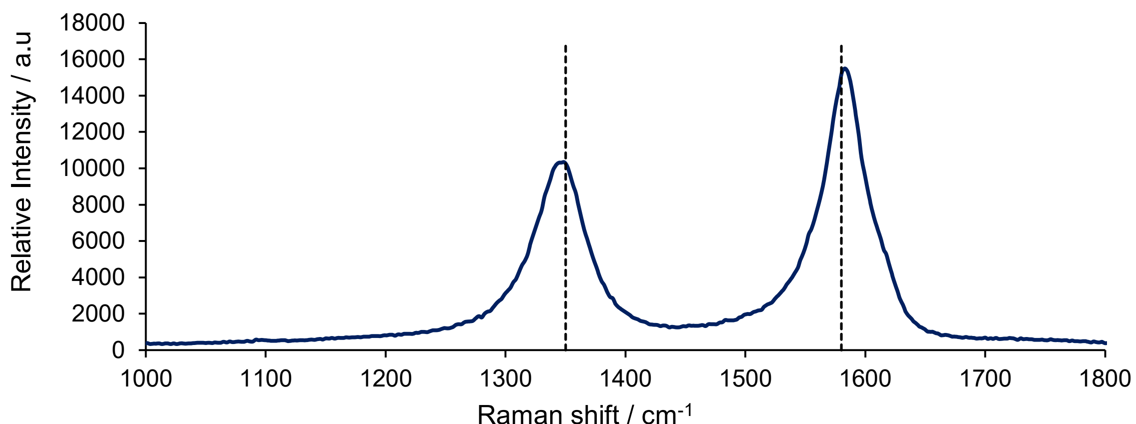

Figure 20 - A Raman of the deposition under the focus plasma arc in Run 3, demonstrating sharp D and G bands at 1350 cm^{-1} and 1580 cm^{-1} respectively. [53]

Initially (Runs 1-3) the plasma periodically collapsed into an arc discharge, Figure 19. The arc discharge was localised on the right-hand side of the substrate, symptomatic of electrodes out of parallel, driving uneven deposition. Surrounding the arc discharge was an area of zero deposition (semi-circle with radius 5 mm)

indicative of hydrogen radicals in the outer plasma sheath rapidly etching sp^2 depositon.[4] Highly ordered graphitic deposits were present under the arc focus, Figure 20. This was demonstrated by the sharp graphite G-band and D-band at 1580 cm^{-1} and 1350 cm^{-1} in the Raman spectrum. The G band suggested crystalline graphite, whereas D-band intense indicated disorder, likely due to defects such as inclusions or grain boundaries.[53]

This growth was more comparable to arc-jet CVD.[4] It was concluded, due to the arc consistently focusing on the same area that the electrodes were out of parallel. To correct this, washers controlling electrode gap were changed to produce more level electrodes.

A Stabilised Plasma (Run 6)

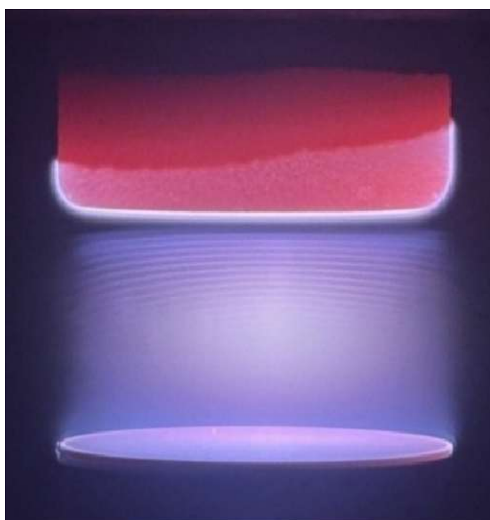

Figure 21 – The stable plasma from Run 6 (175 Torr, 1790 W). Photograph taken by Prof. Neil Fox.

Control of electrode levelling and a lower pressure (175 Torr) produced a stable plasma, Figure 21. Hartmann found an upper pressure limit of 200 Torr due to plasma collapse and a lower pressure limit of 150 Torr, below which plasma glow approached the chamber shielding.[54] This study suggested that an upper pressure limit, for the pulsed-DC reactor in Bristol was 175 Torr, at powers between 1.7 – 2.0 kW. The pressure stability limit was less than Hartmann's. This may have been due to a difference in volume, flow rates, and electrode cooling system compared to that of Hartman, these all contributing factors to the upper pressure limit .[54] Alternatively Electrodes in this study may have been less in parallel. Decreasing the pressure increased the mean free path of radicals within the plasma sheath which in turn expanded to increase lateral coverage of plasma across the electrodes. In subsequent runs the pressure was kept below 175 Torr, within the stability limit.

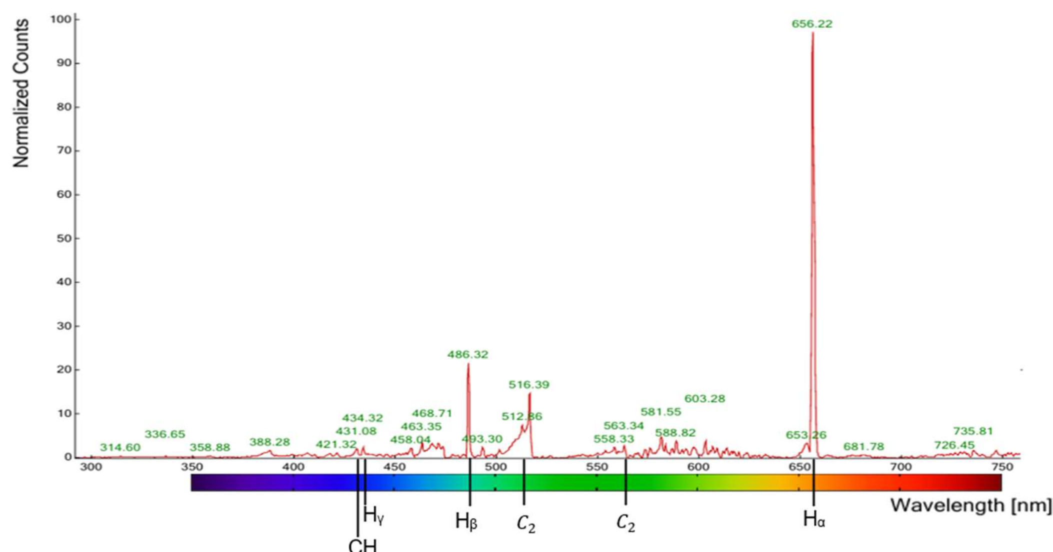

Figure 22 - An Optical emissions spectrum showing H Balmer series, CH species and C_2 Swan bands of the plasma from Run 6, Figure 21.

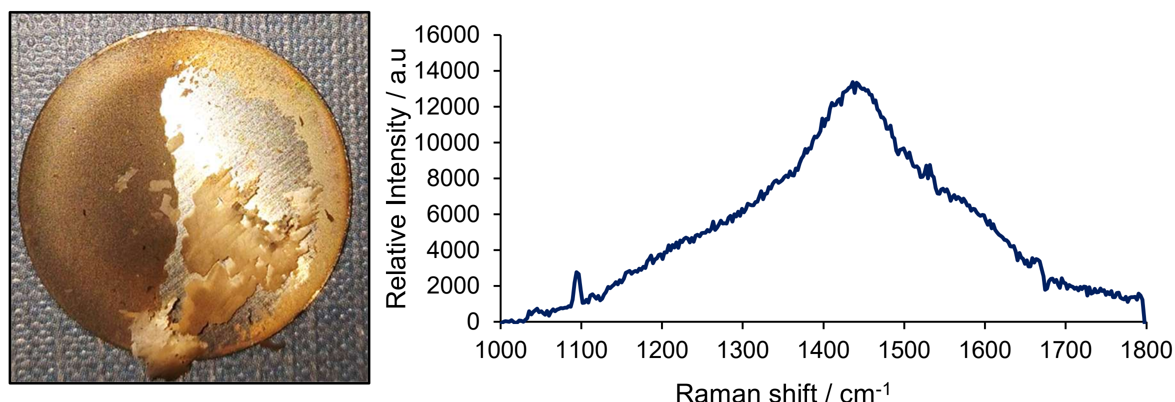

Figure 23 - On the left a highly graphitic film deposited on a 25 mm Mo disk, significant delamination shown. On the right a Raman spectrum with no 1332 cm^{-1} diamond peak present.

Corresponding OES data, Figure 22, taken at 50 minutes exhibited H Balmer series and C_2 swan bands, the latter directly correlated to CH_3 growth species in a relationship proven by Hemawan et al.[45] A peak was present at 388.28 nm, from the N_2^+ (B-X), indicative of nitrogen presence in the chamber potentially due to non-vacuum conditions before growth.[55]

Raman spectroscopy concluded deposition was amorphous carbon with no 1332 cm^{-1} diamond peak. This conclusion was corroborated by the delamination, Figure 23, which would not be expected between a type 3 substrate such as Mo as a strongly adhered carbide layer was formed.[35] Despite poor deposition quality the high plasma stability concluded part one of this study, with an upper pressure limit of 175 Torr identified as a key parameter in prevention of an arc discharge.

Optimisation for Film Quality

Once the plasma was proven to be repeatably stable without arcing, the project focused on improving deposition quality. Novel ways of improving deposition composition without affecting plasma stability were examined. The aim was to control substrate and cathode temperatures independently. Reactor modifications were made, including the addition of a copper mesh, which facilitated a hydrogen 'flush' of the chamber before power-down. This was expected to improve film quality due to hydrogen radicals' preferential etch of sp^2 hybridised carbon over sp^3.[4]

In optimisation for film quality, colour temperature was used as a qualitative guide, the limitations in its accuracy are acknowledged, exacerbated by the presence plasma glow. It was not possible to use a pyrometer as the substrates were too thin (0.5 mm), additionally it was not possible to fit a thermocouple within the timeframe. For these reasons, the following results do not quantify temperature, the associated uncertainty of any values would be too large to be useful. Instead, camera-phone images were used for inter-substrate colour comparisons, exposure decreased to remove plasma glow.

Substrate Temperature

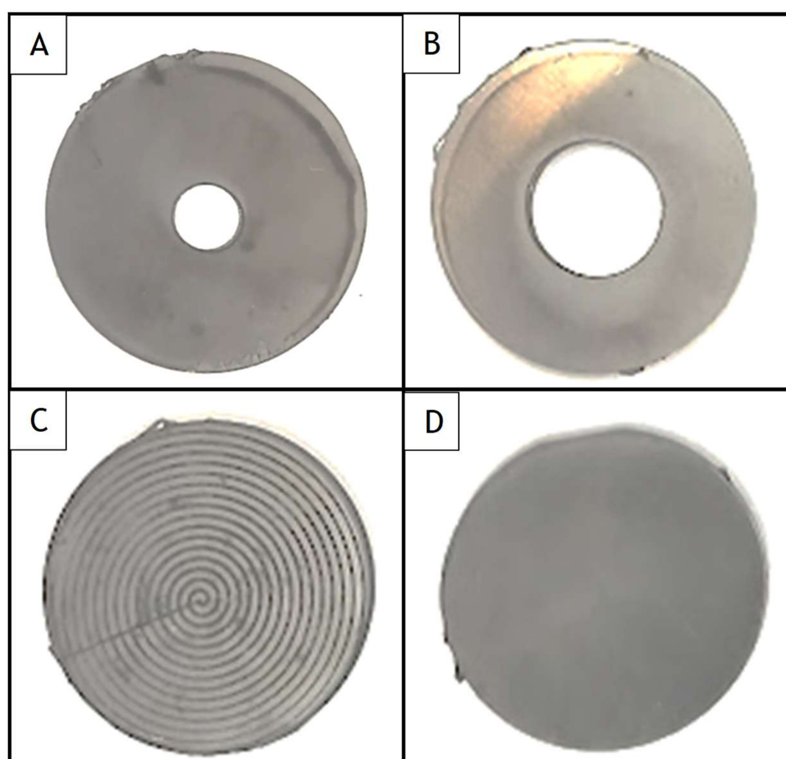

Figure 24 - 0.5 mm thick, 25 mm diameter Mo thermal breaks A to D with 0.16, 4, 15 and 40 % areas missing, respectively.

In Run 6, Figure 21, the substrate did not exceed temperature for stable thermionic emission (glow temperature) of 525 °C. This was despite stacking a second substrate 0.5 mm thick Mo substrate under the first to reduce thermal contact.[56] Substrate temperature for CVD diamond growth must be within 725 – 1125 °C, therefore substrate temperature needed to be increased independently of cathode temperature.[4] It was advised that adjustment to water flow rate of the anode cooling

system was too coarse for this purpose. Thermal breaks, Figure 24, were advised to give finer control of substrate temperature. Thermal breaks had been used successfully in literature with Lee et al used tungsten to break thermal contact between anode and substrate. [34] Additionally Ed Smith had introduced thermal breaks on the Bristol pulsed DC reactor, however these were discarded by subsequent studies then readopted in this project.[57] Annular thermal breaks with 0.15 % (A) and 4 % (B) area missing were cut along with spiral thermal breaks with approximately 15 % (C) and 30 % (D) contact area missing.

An Unsuccessful use of thermal breaks (Run 8)

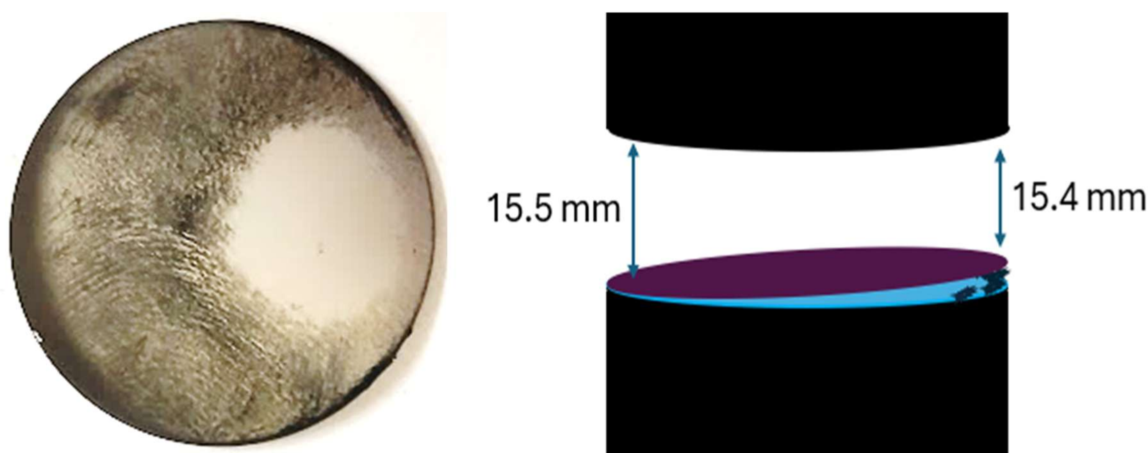

Figure 25 - On the left the uneven deposition on a Mo substrate after 75-minute growth (Run 8) and a diagram of uneven substrate placement due to rough edges on the right.

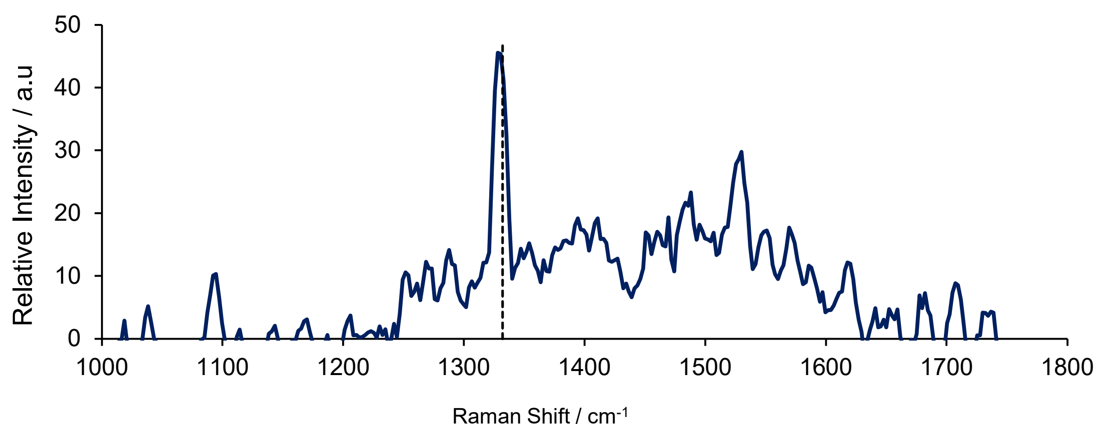

Figure 26 - Raman from centre of the deposition with a diamond peak at 1332 cm^{-1} baseline subtracted and FWHM 5 cm^{-1}

The first use of a thermal break was conducted with A and yielded an anomalous result with a gradient of growth across the substrate, Figure 25. This was likely due to the jagged edges on the thermal break (A) resulting in a substrate lift. The elevated right-hand exceeded thermal glow temperature, while the cooler left had side did not. Nucleation was observed on the cooler side of the substrate; no nucleation was observed on the hotter side. This demonstrated too high a temperature prevented any nucleation. Deposition indicated that the centre of the

substrate was within range for diamond growth. Clusters of ballast type diamond were visible under confocal laser microscopy. Raman, Figure 26, had a significant 1332 cm^{-1} diamond peak, FWHM 5 cm^{-1}. This run was informative to ideal glow temperature as well as testament to the plasma stability these conditions yielded, as despite unevenness the plasma did not collapse into an arc discharge. The jagged edges were removed and thermal breaks reassessed.

The Impact of Thermal Breaks on Substrate Temperature

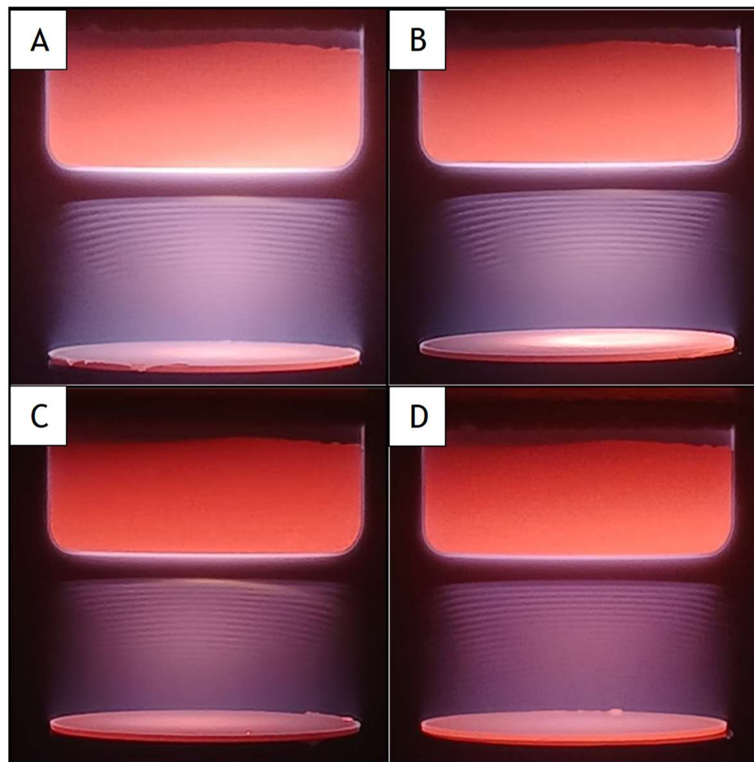

Figure 27 - Images of the plasma from thermal breaks A – D (shown in Figure 22), grown on 25 mm Mo substrates, 15.5 mm electrode gap, 2000 W, 170 Torr.

Substrate colour temperatures corresponding to each thermal break were observed, Figure 27. Raman spectroscopy revealed all deposition was graphitic, with no 1332 cm^{-1} diamond peak present. An orange halo in the plasma at 70 minutes was indicative of the cathode exceeding the 1000 °C maximum growth temperature suggested by Hartmann. [54] This was likely caused by the 2 kW power. It was decided that literature values of optimal substrate temperature range from May of 725 – 1125 °C were to be used with colour temperatures.[4]

Thermal break A, annular with the 0.16 % by area cutout, was below glow temperature, suggesting it was outside the optimum temperature range for growth. Thermal break B with 4 % area missing had a central bare circle accompanied by a gradient in nucleation density (low to high) from the centre to edge. The limited uniformity of annular rings was not observed in studies by Ed Smith, therefore it was likely the thickness of the substrate (0.5 mm compared to 10 mm) limited their ability to transfer heat.[57] This demonstrates the transferability of thermal breaks was limited and suggests a different thermal break would need to be devised for new substrate materials or thicknesses.

Neither spiral thermal break (C or D) exhibited an obvious temperature gradient during growth. So far it had been demonstrated that too high a substrate temperature would result in zero deposition; therefore, thermal break C (15 % area missing) was selected for further runs and D (40 % area missing) was discarded to avoid null runs.

Comparison to between Runs 4 & 14

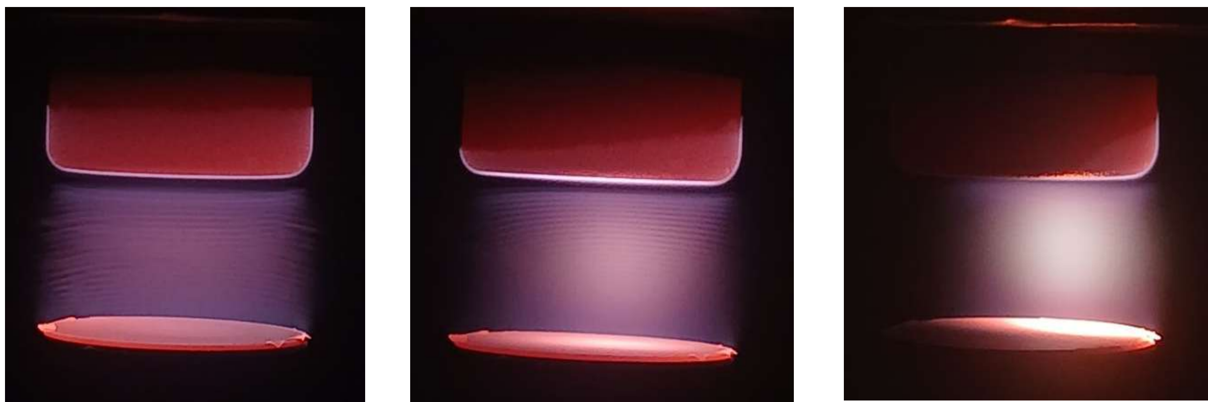

Figure 28 - Progression of an unstable plasma taken at 20, 50 and 70 minutes from left to right. Conditions: 1800 W, 180 Torr,

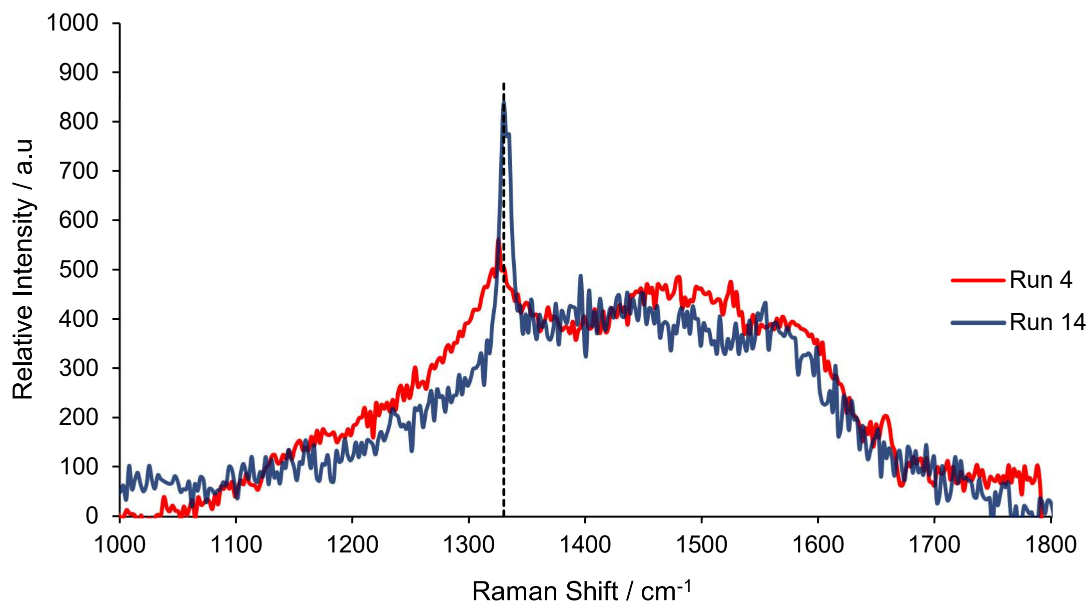

Figure 29 - Raman of Run 14 (blue) compared to Run 4 (red) relative intensity of 1332 cm^{-1} diamond peak higher in Run 14.

Once thermal break C was selected as providing the most even substrate temperature, its efficacy was assessed. Conditions were identical to the 4th run, selected as it was the only run without a thermal break where diamond had been deposited. This validated two key findings. Firstly, that pressure of 180 Torr was too high for a stable plasma as the plasma became highly localised, Figure 28, then arced. Secondly that substrate temperature without a thermal break was too low. The intensity of the Raman peak in Run 14 was higher with a FWHM of 16 cm^{-1}

whereas Run 4 was uncalculatable due to the large amorphous carbon signal, Figure 29.

The plasma in run 14 was observed to begin stable, gradually becoming more localised from 20 minutes to forming a complete arc at 75 minutes. Notable to this instability was the change in both cathode and substrate temperature. Given this thermal break and the Raman and LEXT data being indictive diamond it was thought that substrate temperature was within range for growth, therefore ideally would be unchanged. The plasma appeared to drop, changing from hugging the cathode upon startup to not covering the bottom of the cathode over the duration of the run; once coverage of the cathode was lost so was plasma stability, Figure 28. Whilst the plasma instability was primarily attributed to the higher pressure of 180 Torr, it was speculated that if the 'plasma drop' could be prevented stability could be maintained. Therefore investigations were carried out into the factors causing 'the plasma drop'.

'Plasma Drop' and Cathode Temperature

The observed decrease in plasma stability in run 14 was attributed not only to higher pressure of 180 Torr, but also to due to substrate heating over time. The plasma was observed to shift downwards, hugging the hottest area of the substrate and destabilising the system. Simultaneous to substrate heating (at 50 – 80 minutes) voltage rapidly declined, dropping by 20 V per minute, compared to the otherwise observed 1 V per minute. A study on the same reactor by Ed Smith also saw a sudden voltage drop (unquantified) and cited this as a key factor in premature growth termination.[57]

It was thought that substrate heating caused changes in the gas phase chemistry within the ion sheath. The ion sheath exists at the plasma-substrate boundary, a region in which there was typically a uniform (positive) ion density.[58] Above stable thermionic temperature (glow temperature) secondary thermionic electrons were emitted from the substrate (on the anode). More electrons were emitted in higher temperature regions. The thermionic electron emission is hypothesised to have had two effects: firstly, electrons caused a voltage drop by negatively biasing the anode. Secondly thermionic electrons attracted positive ions in the plasma sheath to shield the plasma column. The increase in ion and electron density surrounding the hotter substrate area may have caused the shift in positive plasma column position.[58] It was thought increased ion bombardment in this area further increased temperature, therefore increased thermionic emission creating a feedback loop.

In contrast, electron emission from the cathode was inherently even, therefore may have promoted isotropy of ions in the plasma column. At lower substrate temperatures, cathode electron emission likely dictated ion isotropy within the plasma column, making the plasma more stable. Across CVD methods ideal substrate temperature was in the range 725 – 1125 °C; in pulsed-DC CVD Hartman stated acceptable cathode temperature range for growth was 900 – 1000 °C.[4, 27] It was hypothesised that maintaining substrate temperature below that of the cathode would cause thermionic emission from cathode to dominate isotropy of ions in the plasma column, therefore causing a more stable plasma.

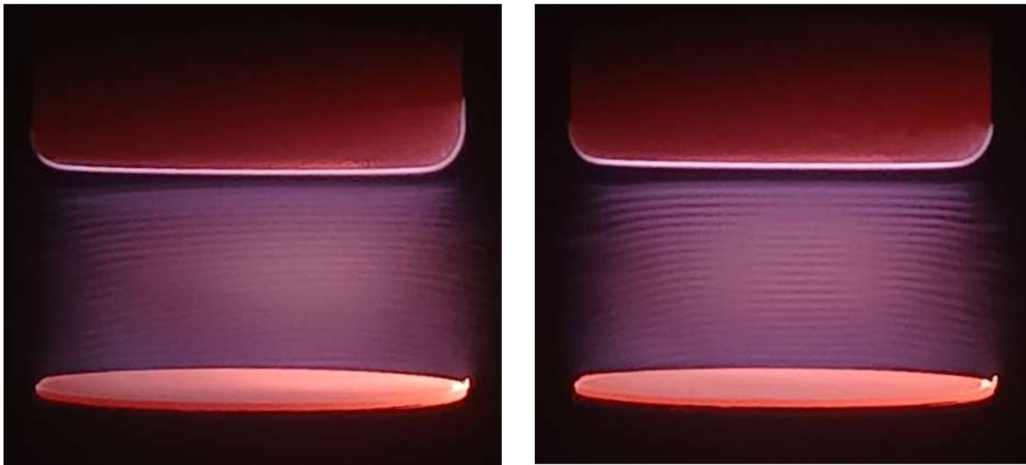

Figure 30 - Effect of cathode temperature on plasma stability Rest time 2.5 μs on left and 1.5 μs on right, exhibiting a hotter cathode and more even substrate at lower rest time, images taken at 90 and 95 minutes. Conditions: 170 Torr 1750 W.

Isolating cathode and anode temperature was challenging; rest time was investigated as a means to do this. It was selected over frequency due to arc discharge formation at strike frequency 100 kHz, as well as simplicity in calculation by maintaining total period as 8 μs. Figure 30 demonstrated successful stabilisation of a plasma though decreasing rest time from 2.5 μs to 1.5 μs, resulting in increasing thermionic emission from cathode. It was also found that increasing rest time instantaneously irradicated the orange halo, caused by too high cathode temperature. This was beneficial as Hartmann described the carbide sputtering and associated poor film quality caused by the orange halo which could be avoided.[54]

Optimised conditions (Run 17)

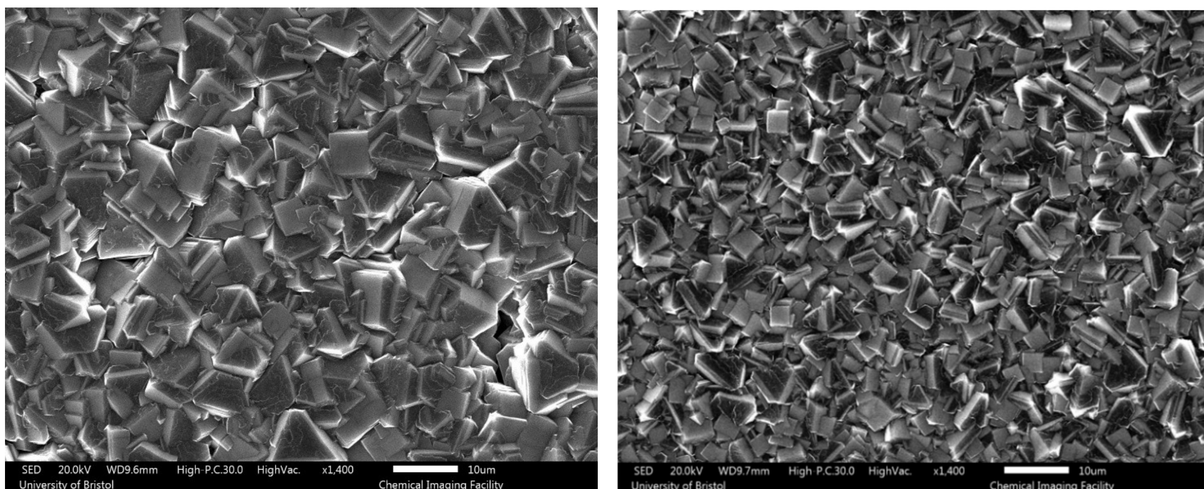

Figure 31 - SEM of areas differing most in morphology, centre (left) vs edge (right) from Run 17

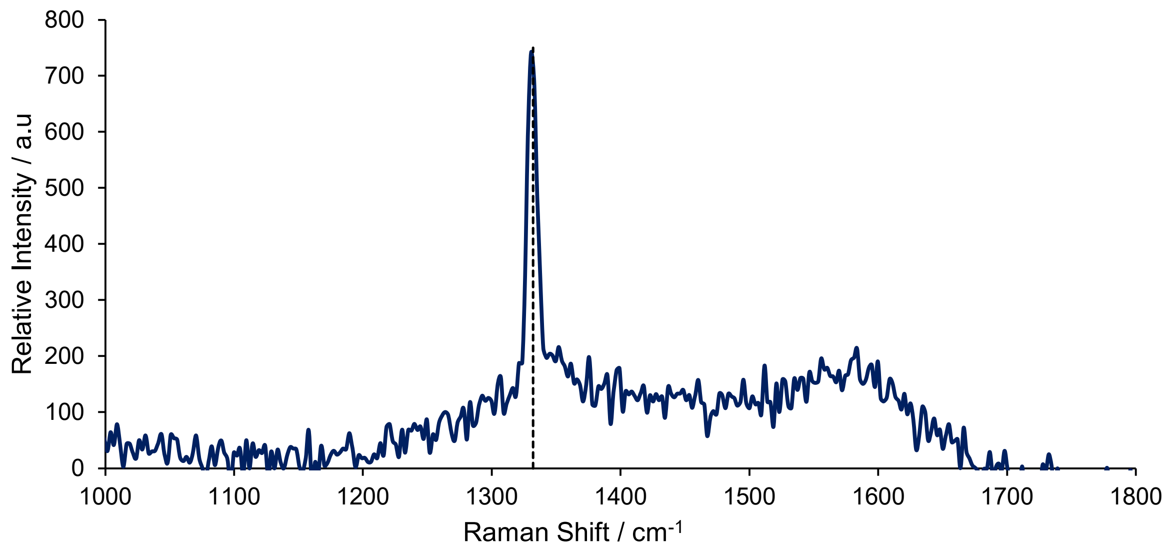

Figure 32 - Raman of resulting optimised film from Run 17, with 1332 cm^{-1} diamond peak (FWHM 9 cm^{-1}).

Runs 15 – 17 focused on variable rest times from 2.8 µs to 1.2 µs of an 8 µs period. The fully optimised growth run (Run 17) maintained plasma stability for the duration, 180 minutes, by decreasing rest time from 2.5 µs to 1.6 µs after 60 minutes. This decrease in rest time increased cathode temperature therefore maintaining a central plasma for reasons detailed above. Run 17 used thermal break C (spiralled 15 % area missing) to keep substrate temperature within recommended growth temperature. SEM images, Figure 31, showed mostly (111) orientated crystals up to 10 µm in length at the centre and 7 µm at the edge. This was indicative of a temperature gradient or a result of changing plasma composition from centre to edge. This deposition was successful with a Raman diamond peak at 1332 cm^{-1} with FWHM 9 cm^{-1} and growth rate 12.4 µm h^{-1}. The Raman, Figure 32, had small amounts of amorphous carbon, likely within the grain boundaries.[27]

Closed Chamber Deposition (Run 18)

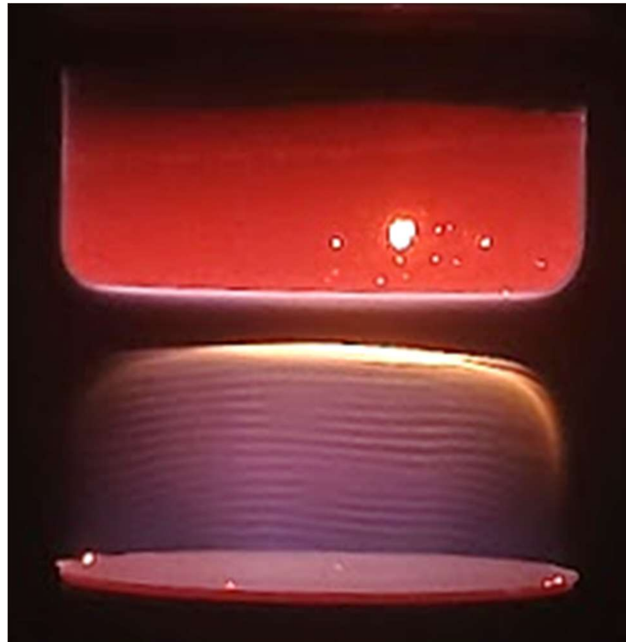

Figure 33 - Plasma photograph of closed chamber run, debris on the cathode and orange halo visible. Image taken at time 160 minutes.

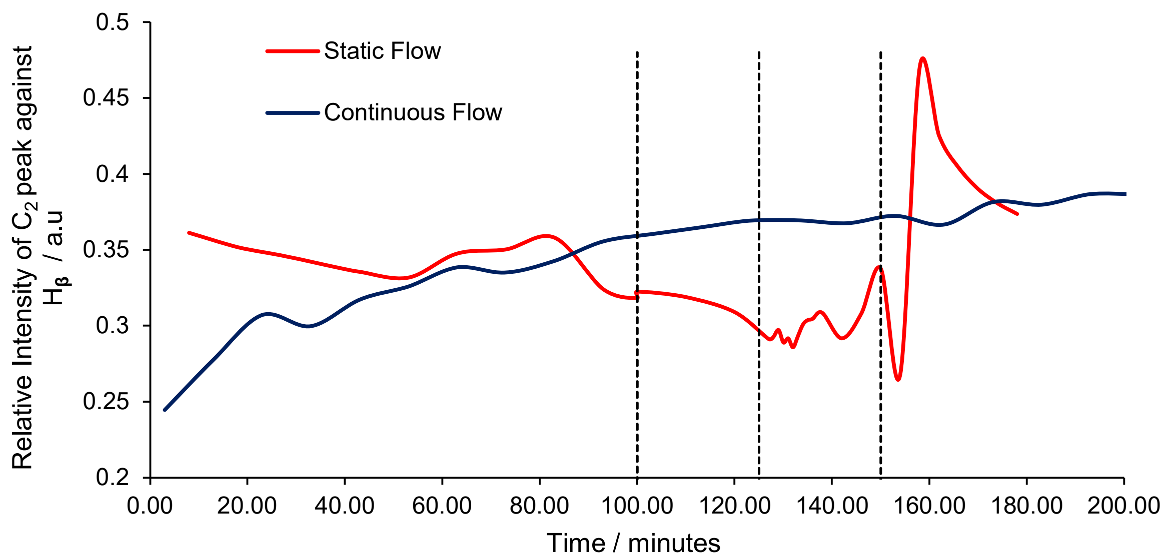

Figure 34 - Intensity of the C_2 peak relative to H_β emission over time from the average of Run 16 and 17 in blue and the closed chamber (run 18) in red.

The plasma behaviour during closed chamber was unusual, Figure 33. Observations during growth were different to continuous flow equivalent this included: a distinctive orange halo, lower substrate temperature, and debris on the cathode. The orange halo appeared after fifteen minutes, remaining for thirty minutes, reappearing because of methane injections during the closed chamber portion.

Additionally, the OES relative intensity of C_2 to Hb, Figure 34, showed unexpected variations. Up to 100 minutes the Run 18 and continuous flow runs were both under continuous gas flow and identical: power, pressure, flow rates, thermal breaks, and rest times, yet a 28 % difference in relative intensities was observed at 5 minutes. This was likely due to amorphous carbon deposits on the electrodes and chamber walls, built up over the prior growth run, then etched by the hydrogen rich plasma. Further evidence for this was the early onset of an orange halo, composed of longer hydrocarbon species, despite low cathode glow temperature. Cleaning the electrodes with isopropyl alcohol (IPA) after a four-hour growth was insufficient, an abrasive cleaning method ought to have been used.

An orange halo appeared after the section methane injection (150 minutes), this was likely due to improper plasma mixing. It was suggested that mixing of heavier species in plasma was less favourable than lighter species. Additionally, C_2/Hb intensity was 30 % higher at its peak that that that observed in continuous flow. This would correspond to 5 % methane concentration, compared to the target 3.8 %, Hartmann correlated higher methane with higher non-diamond carbon deposits.[54]

The orange halo may have functioned as a barrier between cathode and easily excited gas species which usually participate in ion bombardment of the substrate, explaining the lower substrate temperature. Further evidence for this was the 20 V difference between potential difference in runs 17 & 18 at 20 minutes at this point identical other than electrode cleanliness causing orange halo in run 18 as the chamber was still under continuous flow. Additionally, the ‘voltage drop’ when an orange halo appeared early, was delayed by the same duration that the orange halo was present. In run 18 the ‘voltage drop’ occurred twenty minutes later than observed in run 17, twenty minutes was also the duration of the orange halo presence. This barrier effect provides explanation for the lower substrate temperature.

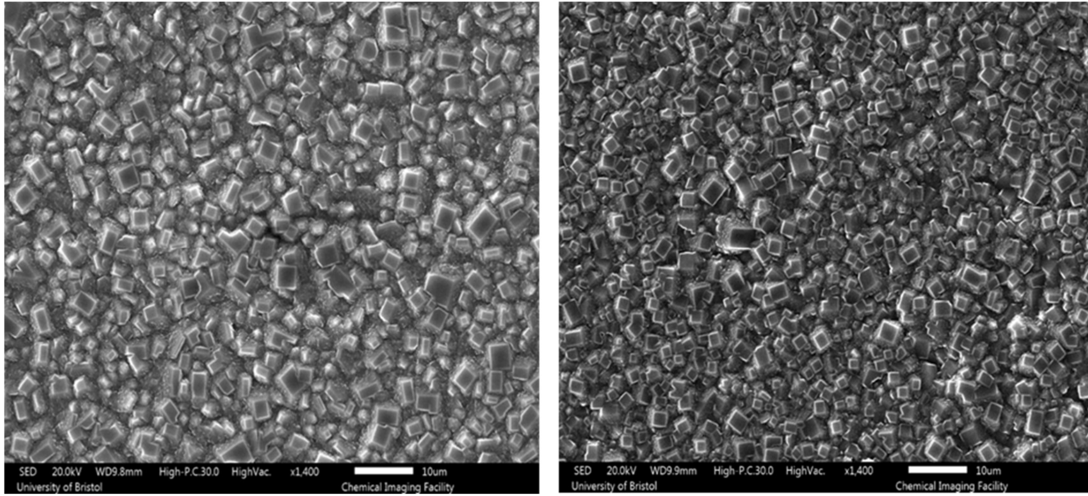

Figure 35 - SEM images of closed chamber growth on Mo substrate showing (100) facets growth of high uniformity from centre (left) to 2 mm from edge (right). Average facet width 3.5 μm

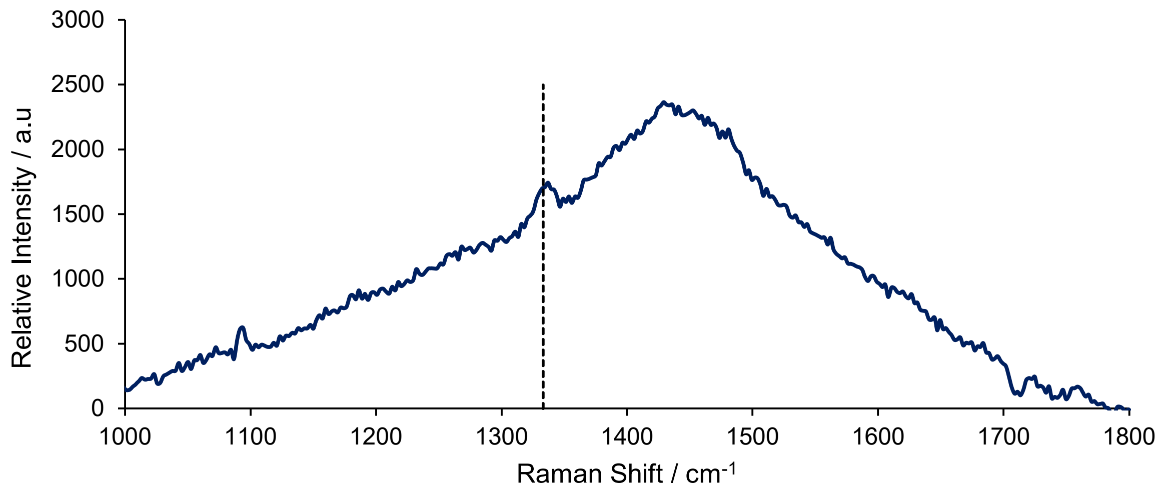

Figure 36 - Raman of deposition from closed chamber run, exhibiting a small 1332 cm^{-1} diamond peak and a large graphitic signal

SEM, Figure 35, showed (100) faceted diamond, average grain width of 3.5 μm, at a growth rate of 4.44 μm h^{-1}. Raman, Figure 36, was largely graphitic with a very small diamond peak. Raman could suggest methane exceeded the 4% and non-diamond carbon was deposited. The hydrogen flush in power-down etched the graphitic deposits, leaving SEM appearing with square facets, however these were likely due to growth before the second methane injection. Hartmann also observed a increase in non-diamond carbon at methane concentrations greater than 4 %, especially at grain boundaries, which were likely emphasised due to low facet size.[27]

Silicon as a Substrate (Run 19)

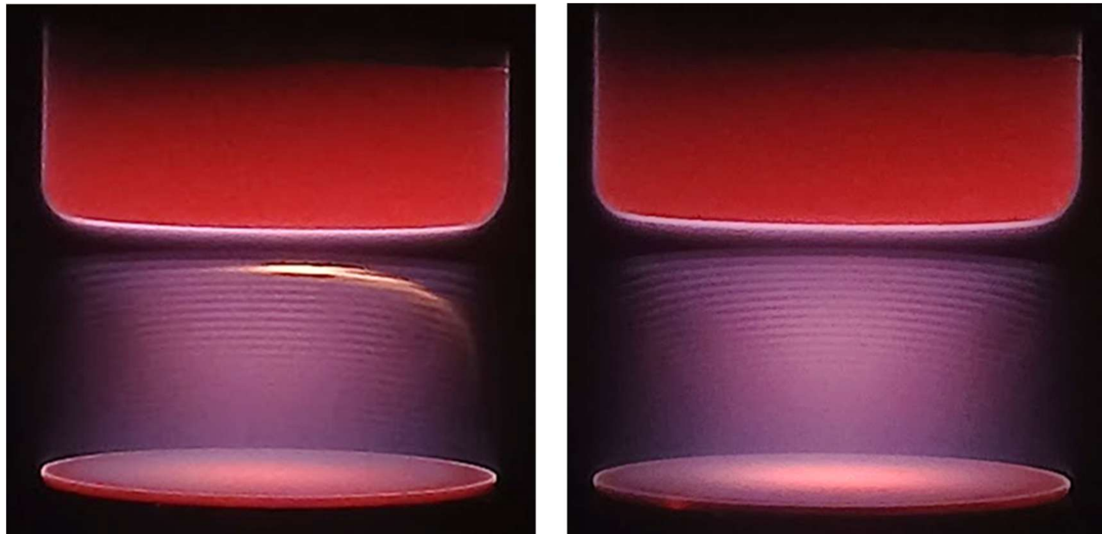

Figure 37 - Plasma images of silicon substrate with T = 2.5 μs left and T = 3.0 μs right, showing localised heating on centre of substrate and disappearance of 'orange halo' with increased cathode cooling through rest time.

P-type silicon was used due to give conductivity at low temperatures and facilitate the start-up procedure. During start-up it was notable that the plasma was contracted to the centre of the substrate as opposed to the even coverage observed in previous runs. During growth a hotspot was present on the silicon substrate, slightly offset from the centre, Figure 37. This may be due to silicon's inferior thermal conductivity relative to that of molybdenum. Alternatively, p-type silicon increasing temperature increased thermal conductivity an inherent property of semiconductors such as silicon.[59] This may have created a feedback loop whereby plasma focused on the hotter centre of the silicon substrate, which in turn was made more conductive therefore attracted the majority of ion bombardment, further heating the substrate and increasing its electrical conductivity.[58, 59] Further evidence for this proposed 'feedback loop' was that despite the pronounced 'hotspot' on the Mo substrates when used in conjunction with an annular thermal break (D), plasma was still uniform across the substrate. This may because Mo, as a metal increased in electrical resistance upon heating opposing the feedback loop.[60] However this was not conclusive evidence as the annular ring itself broke the electrical contact between the centre of the substrate and the electrode. A break in electrical conductivity may have been the reason localised heating of Mo on an annular thermal break, exhibited a significantly more diffuse plasma than the localised heating of a silicon substrate.

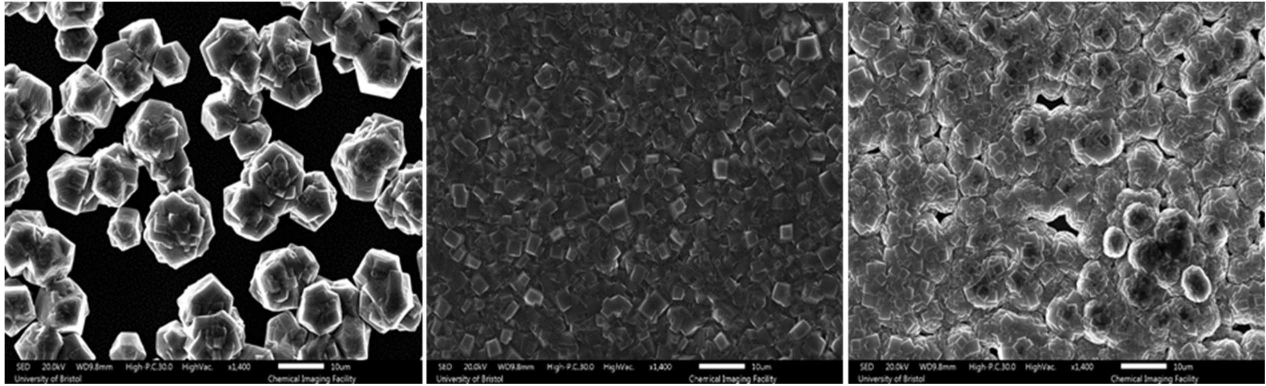

Figure 38 - SEM images of deposition on silicon substrate from centre (left) to edge (right) showing transition from ballast type (111) facet dominated morphologies on hotter edge and centre to (100) morphologies in intermediate (hotter) areas.

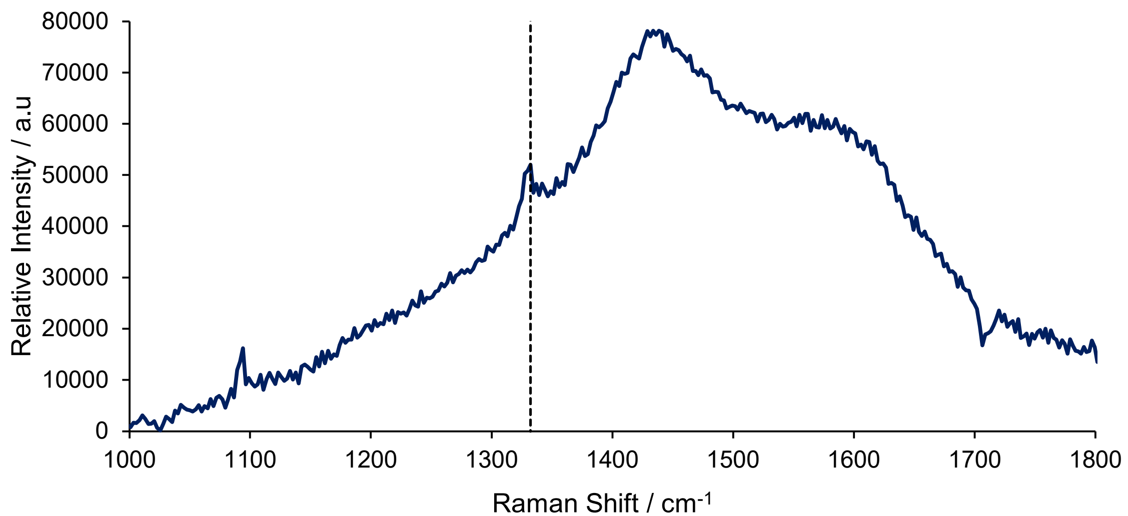

Figure 39 - Raman of deposition on silicon substrate showing small Diamond peak at 1332 cm^{-1}.

The localised heating resulted in different observed morphologies from centre to edge of substrate, Figure 38. Centrally, there was a low nucleation density of ballast-type clusters. 5 mm from the centre of the substrate (radius 12.5 mm) there was complete coverage of (100) morphology diamond with a small facet size of 1.5 μm. The small grain size therefore high density of grain boundaries resulted in a Raman with small diamond peak, swamped by graphitic bands, Figure 39. The low 6.28 μm h^{-1} growth rate may a result of lower film quality therefore increased etch by the 10-minute hydrogen flush.

Morphological Comparisons

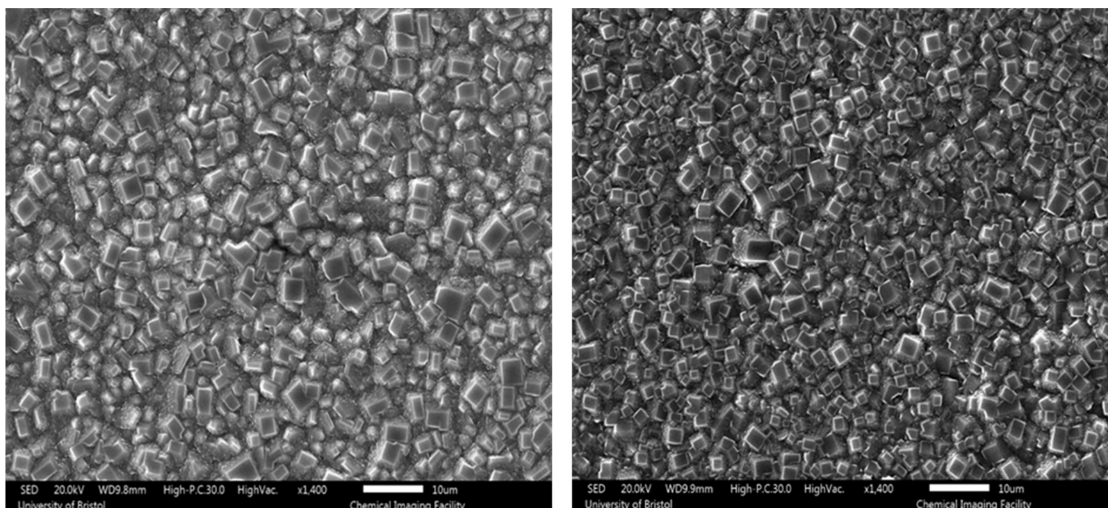

Figure 40 - Comparison of (100) facets from run 16 (left) to run 18 (closed chamber run on right) confocal microscope images 50 × zoom

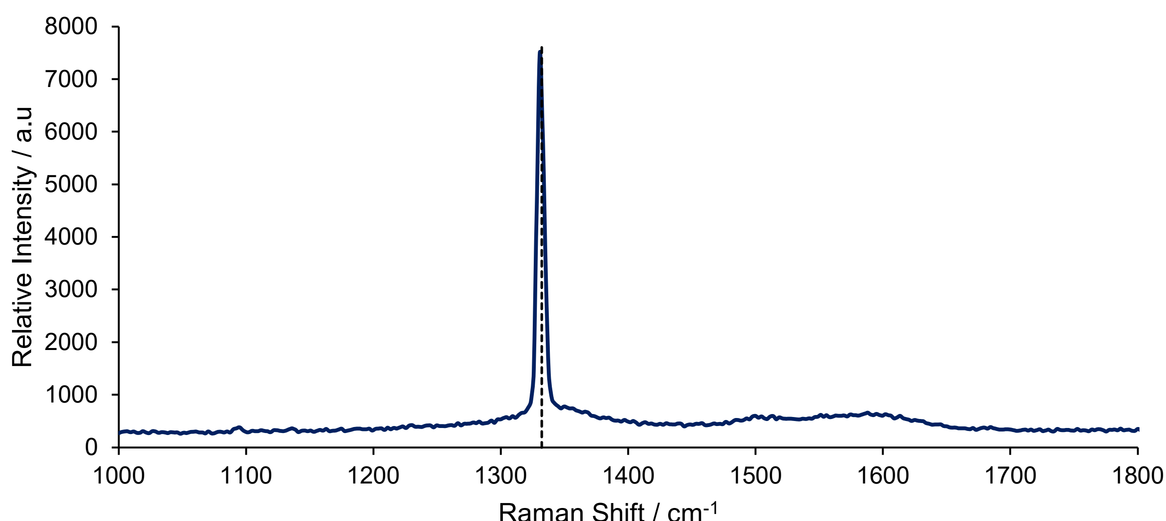

Figure 41 - Run 16, Raman of square faceted diamond sharp 1332 cm^{-1} peak (FWHM 4 cm^{-1})

The two growth runs which achieved square (100) or (110) facets over significant substrate areas were run 16 (whilst optimising rest time), and the close chamber (run 18) these are shown in Figure 40. Similarities in these runs included lower observed substrate temperature and potentially a lower methane, or associated carbon-containing radical concentration. Run 16 despite its excellent Raman, Figure 41, showed low uniformity across the substrate due to localised heating, with the cooler area approximately 50 % of substrate areas, exhibiting (100) morphology. It was also considered that a lower CH growth species density within the plasma caused (100) as it occurred during closed chamber (Run 18) and at the not under the central point of the plasma sheath (Run 16). This theory was opposed by Hartmann who found that at 3 % methane concertation within the gas mixture (111) facets were favoured, whereas at 4 % methane concentration (100) grain orientation was favoured.[54] Therefore cooler substrate temperature likely led to (110) or (100) facet orientation, where higher led to (111), findings supported by Palubiski on the same reactor at higher power.[22]

Conclusions

Pulsed DC CVD was used to grow diamond thin films due to the technique's superiority in heteroepitaxial growth without seeding, as well as large-area deposition capabilities. In this technique, a voltage breakdown was applied across the electrode gap, forming a plasma from the CH_4/ H_2 gas mixture. The substrate (490 mm^2 disk) was positioned on the anode, and ion bombardment by radicals in the plasma caused deposition of either amorphous carbon or diamond. Modifications to the electrode cooling system were made prior to this study, rendering optimised power and pressure from previous studies non-conducive to diamond growth. Previous studies emphasised the tendency of the plasma in this reactor to collapse into arc discharge, a major limiting factor for growth duration and deposition quality. This project aimed to use iterative optimisation to find conditions for diamond deposition, prioritising high plasma-stability. Further aims were to achieve closed chamber growth of isotopically pure diamond and transfer growth conditions to silicon substrates. Raman spectroscopy and Confocal Laser microscopy were used to assess deposition quality.

Two challenges were addressed through this project: plasma stability and cathode-anode temperature interdependence. Initially, to address plasma instability, the upper pressure stability limit was found to be 175 Torr with powers up to 2000 W, providing electrode alignment was within 1°. Cathode and anode temperature were interdependent. This was problematic as the cathode exceeded optimum growth temperature, whereas the substrate, on anode, was below glow temperature of 525 °C, therefore significantly below optimum growth temperature 725 – 1125 °C.[4, 56] Investigation into thermal breaks found a spiral thermal break with 15 % area missing reduced anode-substrate contact sufficiently so the glow temperature of the substrate was within diamond deposition temperature range.

As growth runs progressed substrate temperature increased, to address this a novel investigation into 'rest time' was conducted at rest times between 15 and 44 % of duty cycle. A decrease in 'rest time' heated the cathode, increasing plasma stability and vice versa. A new methodology of variable rest time to control substrate and cathode temperature was adopted to maintain plasma stability. Varying 'rest time' had an instant effect on cathode temperature, therefore was successful in bringing a plasma out of an arc discharge.

In continuous flow growth on Mo conditions of 3.8 % CH_4, 170 Torr and 1800 W were used, accompanied by a 15 % reduction in anode-substrate contact area through a thermal break and pulse time change from 2.5 μs to 1.6 μs at 60 minutes. This resulted in a high uniformity, (111) diamond film with Raman peak at 1332 cm^{-1} (FWHM 9 cm^{-1}). Growth rate was 12.4 μm h^{-1} on a 490 mm^2 deposition area. These results are within range of Hartman's at 4 % methane, which achieved 6 cm^{-1} FWHM and 16 μm h^{-1} growth rate. [54]

Closed chamber growth resulted in an even film with (100) facet orientation, yet Raman spectroscopy exhibited a large graphitic G band and low intensity 1332 cm^{-1} diamond peak. This was likely due to amorphous carbon deposition, after a methane injection, as OES demonstrated a C_2 /Hb intensity 30 % higher at its peak that that that observed in continuous flow. This would correspond to 5 % methane concentration, compared to the target 3.8 %, Hartman correlated higher methane

with higher non-diamond carbon deposits.[27] Time constraints meant that the aim of isotopically pure diamond growth was not achieved.

It was previously thought deposition on silicon substrates was not feasible in this reactor. One growth was conducted on a p-type silicon substrate. Conditions were 1750 W, 170 Torr, 125 kHz and T = 2.5 μs increased to 2.9 μs at 90 minutes, due to cathode heating. Raman demonstrated 1332 cm^{-1} diamond deposition was present, with a small peak relative to the graphitic G band. SEM showed varied morphologies with ballast type diamond then (100) facets followed by further ballast-type from centre to edge. It was likely that substrate temperature dictated film morphology. This experiment demonstrated that conditions optimised for Mo substrates were gentle enough not to melt silicon. It provided evidence that deposition on silicon substrates was possible in this pulsed DC reactor. Changing 'rest time' facilitated this growth, removing orange halo when cathode became too hot and preventing substrate melting.

Finally, morphological comparisons suggested a lower substrate temperature favoured (100) whereas higher temperatures favoured a higher growth rate and triangular (111) facets.

Future work

There were many avenues of future research suggested by this project. Optimising growth on silicon would facilitate production free-standing diamond films. A logical first step would be determining if temperature gradient of the silicon substrate was due to the lower thermal conductivity (relative to Mo) or the relationship between electrical conductivity and temperature of a semiconductor causing plasma distortion. This could be actualised through use of a lower thermal conductivity metal substrate, such as titanium.

The investigation into 'rest time' occurred after the investigation into thermal breaks, therefore the effect of rest time was not explored independent of thermal break C (spiralled, 15 % areas missing). This was an oversight of the work. Given more time, it may be possible that controlling 'rest time' negates the need for a thermal break. The aim of a thermal break was to provide control of substrate temperature independent of cathode temperature. 'Rest time' controlled the position of the plasma relative to each electrode, which provided an inverse relationship between their respective temperatures. Therefore, it may be possible to discard the thermal break, which could in turn increase uniformity of growth on silicon substrates.

Regarding closed chamber runs; future work should focus on decreasing the time taken for chamber to reach steady state. The current procedure is not economical for expensive isotopically pure methane due to the hour of continuous flow required before the chamber was closed.

Furthermore, the conditions detailed in this report were functional but not necessarily fully optimised, and growth rates were not given consideration during optimisation. At this point a Taguchi optimisation within the narrow bounds of plasma stability would be useful to better understand the effects of power and pressure.

Finally, this work was limited by its over-reliance on glow temperature. Installation of a thermocouple would allow a more comprehensive understanding of the effect of substrate temperature on film morphology. This could be combined with variable rest time to create highly tuneable film morphologies.

References

1. D. Das, S. Yaragalla, R. Mishra, S. Thomas, N. Kalarikkal and H. J. Maria, *Carbon-Based Nanofillers Their Rubber Nanocompos.,* Elsevier, 2019, pp. 123-181,
2. S. C. F. Tennant, *Philos. Trans. R. Soc., A*1797, **87**, 123-127.
3. R. Zulkharnay and P. W. May, *Functional Diamond*, 2024, **4**, 2410160.
4. P. W. May, *Philosophical Transactions: Mathematical, Physical and Engineering Sciences*, 2000, **358**, 473-495.
5. J. Zhang, J. Wang, G. Zhang, Z. Huo, Z. Huang and L. Wu, *Mater. Des.*, 2024, **237**, 112577.
6. E. S. Etz, W. S. Hurst and A. Feldman, *J. Mater. Res.*, 2001, **16**, 1694-1711.
7. A. Deneuville, C. E. Nebel and J. Ristein, *Semicond. Semimetals*, Elsevier, 2003, vol. 76, pp. 183-238.
8. R. Sengupta, M. Bhattacharya, S. Bandyopadhyay and A. K. Bhowmick, *Prog. Polym. Sci.*, 2011, **36**, 638-670.
9. A. Victor, *J. Chem. Phys.*, 1962, **36**, 1903-1911.
10. E. O'Bannon, G. Xia, F. Shi, R. Wirth, A. King and L. Dobrzhinetskaya, *Diamond Relat. Mater.*, 2020, **108**, 107876.
11. J. Scott, *Waikato Journal of Education*, 2014, **19**. 47-54
12. S. S. Dossa, I. Ponomarev, B. N. Feigelson, M. Hainke, C. Kranert, J. Friedrich and J. J. Derby, *J. Cryst. Growth*, 2023, **609**, 127150.
13. R. Balmer, J. Brandon, S. Clewes, H. Dhillon, J. Dodson, I. Friel, P. Inglis, T. Madgwick, M. Markham, T. Mollart, N. Perkins, G. Scarsbrook, D. Twitchen, A. Whitehead, J. Wilman and S. Woollard, *J. Phys.: Condens. Matter*, 2009, **21**, 364221.
14. E. M. Smith and W. Wang, *Diamond Relat. Mater.*, 2016, **68**, 10-12.
15. J. Guignard, M. Prakasam and A. Largeteau, *Materials*, 2022, **15**, 2198.
16. T. R. Anthony, in *Diamond and Diamond-like Films and Coatings*, Springer US, Boston, MA, 1991, DOI: 10.1007/978-1-4684-5967-8_36, pp. 555-577.
17. J. C. Angus, A. Argoitia, R. Gat, Z. Li, M. Sunkara, L. Wang and Y. Wang, *Philos. Trans. R. Soc., A*, 1993, **342**, 195-208.
18. J. C. Angus, H. A. Will and W. S. Stanko, *J. Appl. Phys.*, 1968, **39**, 2915-2922.
19. S. Mandal, *RSC Adv.*, 2021, **11**, 10159-10182.
20. E. Uhlmann and J. Koenig, *CIRP Annals*, 2009, **58**, 65-68.
21. J. E. Butler and A. V. Sumant, *Chem. Vap. Deposition*, 2008, **14**, 145-160.
22. D. Palubiski, Doctor of Philosophy, University of Bristol, 2021.
23. P. W. May and R. Zulkharnay, *Philos. Trans. R. Soc., A* , 2025, **383**.
24. P. K. Bachmann, D. Leers and H. Lydtin, *Diamond Relat. Mater.*, 1991, **1**, 1-12.
25. F. Silva, X. Bonnin, J. Scharpf and A. Pasquarelli, *Diamond Relat. Mater.*, 2010, **19**, 397-403.
26. S. Sciortino, S. Lagomarsino, F. Pieralli, E. Borchi and E. Galvanetto, *Diamond Relat. Mater.*, 2002, **11**, 573-578.
27. P. Hartmann, R. Haubner and B. Lux, *Diamond Relat. Mater.*, 1996, **5**, 850-856.
28. T. G. Finn, B. L. Carnahan, W. C. Wells and E. C. Zipf, *J. Chem. Phys.,* 1975, **63**, 1596-1604.

29. P. Mathew, J. George, S. T and P. Kurian, *AIP Adv.*, 2019, **9**, 025215.
30. M. A. Lieberman and A. J. Lichtenberg, in *Principles of Plasma Discharges and Materials Processing*, Springer, 2005, ch. 14, pp. 535–569,
31. M. Nesládek, *Diamond Relat. Mater.*, 1993, **2**, 357-360.
32. D. Lundin and K. Sarakinos, *J. Mater. Res.*, 2012, **27**, 780-792.
33. D. Lundin and H. Pedersen, *Phys. Procedia*, 2013, **46**, 3-11.
34. H.-J. Lee, H. Li, H. Jeon and W.-S. Lee, *Diamond Relat. Mater.*, 2010, **19**, 1393-1400.
35. J. Gracio, Q. Fan and J. Mendes, *J. Phys. D: Appl. Phys.*, 2010, **43**, 374017.
36. L. Velardi, G. Cicala, A. Della Torre, L. N. Francioso and M. A. Signore, *Surfaces*, 2025, **8**, 85.
37. M. Noda, A. Marui, T. Suzuki and M. Umeno, *Diamond Relat. Mater.*, 2005, **14**, 1757-1760.
38. M. L. V. Gayler, *Nature*, 1938, **142**, 478-478.
39. F. Zhou, X. Zhao, W. Chen, J. Hu, P. Xiao, J. Liu, S. Lei, X. Li and S. Zhong, *J. Energy Storage*, 2025, **138**, 118706.
40. M. D. Whitfield, J. A. Savage and R. B. Jackman, *Diamond Relat. Mater.*, 2000, **9**, 262-268.
41. W. F. Banholzer and T. R. Anthony, *Thin Solid Films*, 1992, **212**, 1-10.
42. A. V. Inyushkin, V. G. Ralchenko, A. P. Bolshakov, A. A. Khomich, D. A. Chernodubov, A. N. Taldenkov, V. V. Saraykin and S. Y. Kilin, *J. Appl. Phys.*, 2025, **137**, 125109.
43. A. Billings, MSci, University of Bristol, 2019.
44. H. Harris, MSci, University of Bristol, 2018.
45. K. W. Hemawan and R. J. Hemley, *J. Vac. Sci.Technol., A,* 2015, **33**, 061302.
46. T. B. Settersten, R. L. Farrow and J. A. Gray, *Chem. Phys. Lett.*, 2003, **370**, 204-210.
47. A. Croot, E. J. D. Mahoney, H. Dominguez-Andrade, M. N. R. Ashfold and N. A. Fox, *Diamond Relat. Mater.*, 2020, **109**, 108011.
48. A. D. Elliott, *Curr. Protoc. Cytom.*, 2020, **92**, e68.
49. M. Tare, O. Puli, S. Oros and A. Singh, *Population Data Information Service*, 2009, **92**, 174-180.
50. D. K. Singh, A. Kumar Mishra and A. Materny, *Raman spectroscopy : advances and applications*, Springer, Singapore, 2024.
51. J. Stondus, MSc Thesis, Banaras Hindu University, 2016.
52. C. V. Raman and K. S. Krishnan, *Nature*, 1928, **121**, 501-502.
53. V. Thapliyal, M. E. Alabdulkarim, D. R. Whelan, B. Mainali and J. L. Maxwell, *Diamond Relat. Mater.*, 2022, **127**, 109180.
54. P. Hartmann, R. Haubner and B. Lux, *Int. J. Refract. Met. Hard Mater.*, 1998, **16**, 207-216.
55. M. Wnukowski, P. Jamróz and L. Niedzwiecki, *Int. J. Hydrogen Energy*, 2023, **48**, 11640-11651.
56. J. W. Draper, *Philos. Mag.* , 1847, **30**, 345-360.
57. E. Smith, MSc Thesis, University of Bristol, 2017.
58. M. A. Lieberman and A. J. Lichtenberg, in *Principles of Plasma Discharges and Materials Processing*, Springer, 2005, ch. 6, pp. 165–206
59. K. Y. Tsao and C. T. Sah, *Solid-State Electron.*, 1976, **19**, 949-953.
60. L. Guo, X. Liu, J. Zhang, H. Zhang, X. Gu, L. Lu, H. Zhang and J. Zhan, *Int. J. Refract. Met. Hard Mater.*,, 2026, **134**, 107451.

Appendix

MFC Testing

Time taken for pressure to increase from 15 to 20 Torr was measured at varied flow rates at each MFC. Argon and Methane had maximum flow 200 so were calibrated with flow rates 50, 100, 150 and 200 sccm. Hydrogen had maximum flow 2000 sccm so was calibrated at flow rates 400, 500, 600, 1000 and 1500 sccm. Additional calibration was carried out for methane at flow rates 15, 20, 15 and 30 sccm, to ensure reliability at the flow rates used during growth.

All calibrations produced linear correlation. They did not pass through the origin, it was deemed this is due to a low leak rate of 0.02 Torr h^{-1} across the chamber and line. The working maximum flow rate for the hydrogen MFC was deemed 1000 sccm, as at 1500 sccm setpoint, flow rate could not stabilise.

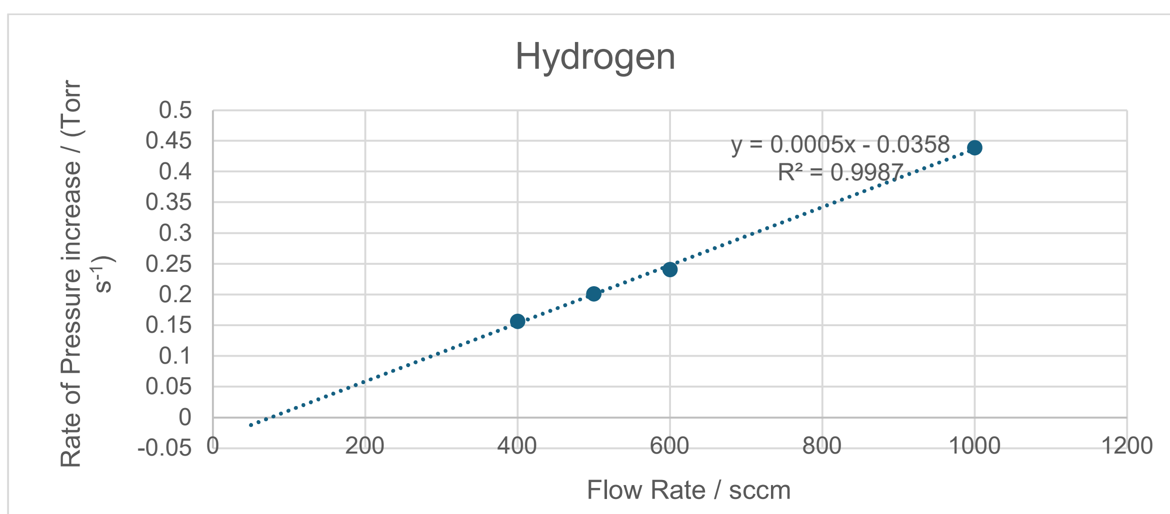

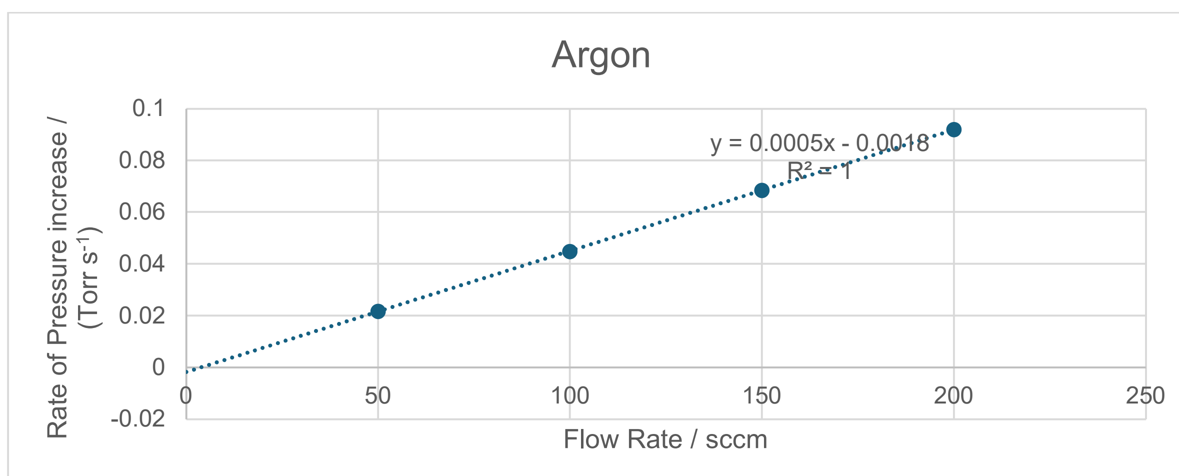

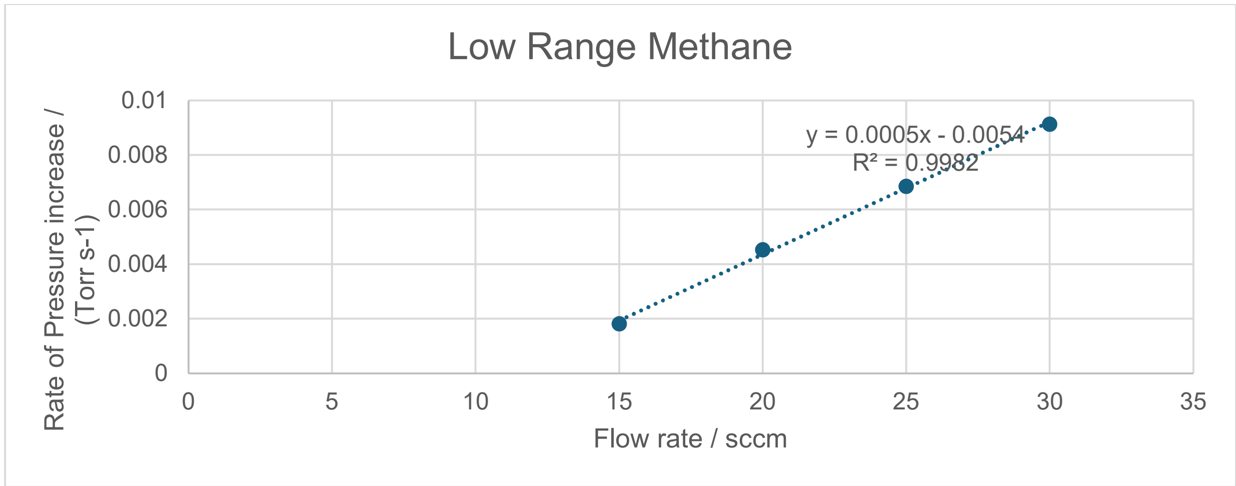
Low Range Methane
Rate of Pressure increase / (Torr s-1)
0.01
0.008
0.006
0.004
0.002
0
0
5
10
15
20
25
30
35
Flow rate / sccm
y = 0.0005x - 0.0054
R² = 0.9982

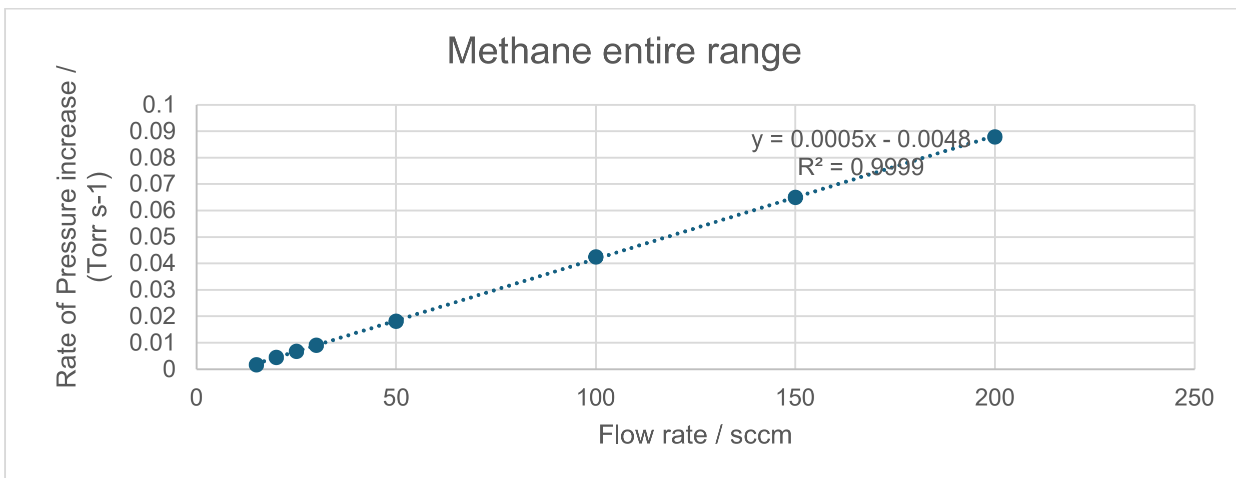
Methane entire range
Rate of Pressure increase / (Torr s-1)
0.1
0.09
0.08
0.07
0.06
0.05
0.04
0.03
0.02
0.01
0
0
50
100
150
200
250
Flow rate / sccm
y = 0.0005x - 0.0048
R² = 0.9999

Complete Run Results Summary

Run	Diamond grown
1 – F = 100kHz	no - Arcing
2	no - Arcing
3	No - concentrated arc
4	Yes, uneven
5	Yes but plasma was uneven
6	No but plasma was very even
7	no
8	Yes - but substrate tilt
9	No
10	
11	No
12	Yes, only edge
13	No
14	Yes, throughout however better quality next to arc
15	Yes, but limited
16	Yes but lopsided plasma
17	Yes
18*	Yes, high uniformity
19**	Yes - less in centre

Images of Depositions from Each Run